Integration of an Optical Coherence Tomography Subsystem on Silicon on Insulator

Semere Ayalew Tadesse

Promotoren: prof. dr. ir. Roel Baets, prof. dr. ir. Patrick Segers
Begeleider: ir. Günay Yurtsever

Scriptie ingediend tot het behalen van de academische graad van

Vakgroep Informatietechnologie
Voorzitter: prof. dr. ir. Paul Lagasse

Vakgroep Civiele techniek
Voorzitter: prof. dr. ir. Julien De Rouck

Faculteit Ingenieurswetenschappen
Academiejaar 2007-2008

UNIVERSITEIT GENT

Toelating tot bruikleen

De auteur de toelating dit afstudeerwerk voor consultative beschikkbaar te stellen en de-len van het afstudeerwerk te copieren voor persoonlijk gebruik. Elk ander gebruik valt onder de beperkingen van het auteeursrecht, in het bijzonder met betrekking tot de verplichting de bron uitdrukkelijk te vermelden bij het aanhalen van resultaten uit afstudeerwerk.

Permission for usage (English version)

The author gives his permission to make this work available for consultation and to copy parts of the work for personal use. Any other use is bound to the restrictions of copyright legislation, in particular regarding the obligation to specify the source when using the results of this work.

Semere Ayalew Tadesse

10th June 2008

Acknowledgments

I would like to thank the Erasmus Mundus Master of Photonics Consortium for giving me the financial support to pursue my education. I am thankful to my promoters Prof.dr.ir. Roel Baets and Prof. dr. ir. Patrick Segers for giving me the chance to work on this problem. I wish to express my gratitude to my supervisor ir. Gunay Yurtsever for his help, advice and patience as we have discussed the many challenges that I have faced in carrying out this research. I learned a lot from him. Special thanks also goes to ir. Joost Brouckaert for his generous support, and helping me find out answers for my problems. I thank my colleagues for helpful discussions in my research work. Finally, my thank goes to my family for their support and advice.

Abstract

This thesis presents the miniaturization of Optical Coherence Tomography (OCT) on a Silicon-on-Insulator based photonic integrated circuit. We designed a Mach-Zehnder interferometer based Fourier- Domain OCT on a photonic chip. The key components of the circuit are the spectrometer, the probing element, and the reflection collection component. A planar Concave Grating (PCG) was used as the spectrometer component of the circuit. The designed PCG demultiplexer has a channel spacing of 1nm, and 50 output channels. The wavelength resolution gives an OCT measurement range of $300\mu m$. The 50nm bandwidth enables an axial resolution of $15\mu m$. The free spectral range of the PCG is *115nm* well above its bandwidth. The linear dispersion is $5.5\mu m/nm$.

We studied the potential of a Focusing Grating Coupler (FGC) to constitute the probing element of the OCT system. The FGC couples the light out of the chip and focuses it to the sample to be imaged. The outcoupling efficiency, the focusing performance, and the aberration properties of the FGC are simulated. The designed PCG has a size of $40\mu m \times 40\mu m$. Its focal length is $350\mu m$. The outcoupled beam has a width of $12.5\mu m$, which is equivalent to the lateral resolution of the OCT.

The designed photonic circuit is fabricated using CMOS fabrication tools that are adapted to SOI photonic platform. The circuit has a total foot print of $6mm \times 2.1mm$, out of which the PCG spectrometer resides on an $5.0mm \times 2.1mm$ area. We characterized the fabricated chip. The PCG demultiplexer gives relatively good results for longer wavelength channels, but the shorter wavelength channel responses show discrepancy from the simulated result. The measurement of the OCT system didn't enable to give OCT signal that can be distinguished from the measured background signal without mounting the sample.

Key words: Fourier-domain optical coherence tomography, silicon -on-insulator, integrated photonic IC, planar concave grating, focusing grating coupler

Integration of an Optical Coherence Tomography subsystem on Silicon-on-Insulator

Semere Ayalew Tadesse

Promoters: Prof. dr.ir. Roel Baets, Prof. dr.ir. Patrick Segers

Supervisor: ir. Gunay Yurtsever

Abstract: In this article we explore the possibilities of implementing Fourier Domain Optical Coherence Tomography on photonic integrated circuit based on a Silicon-on-Insulator material system.

Key words: Optical coherence tomography, silicon-on-insulator, photonic integrated circuit.

I Introduction

Optical Coherence Tomography (OCT) is an imaging technique that is analogous to ultrasound imaging except that it uses light echoes rather than sound. It enables high speed, high resolution, cross-sectional imaging of internal structures in materials. It has been shown that spectral domain (Fourier domain) realizations of OCT have better sensitivity that of time domain OCT systems [1]. In a FD-OCT light beam reflected from sample and reference arms of an interferometer are combined to obtain a spectral interferogram. Reflectivity profile of the sample can be obtained by taking the Fourier transform of the interferogram. Fourier domain OCT does not require any moving parts or phase shifters and has a potential to be implemented as a photonic integrated circuit.

II FD-OCT on photonic IC

Photonics Research Group at Gent University has a wide expertise in nano-photonic Silicon-on-insulator (SOI) platform. Many photonic components such as waveguides, splitters, couplers, and wavelength selective structures have been implemented by our group [2]. We implemented a Mach-Zehnder interferometer based FD-OCT system on an SOI based nanophotonic circuit, the design is shown in Figure 1.

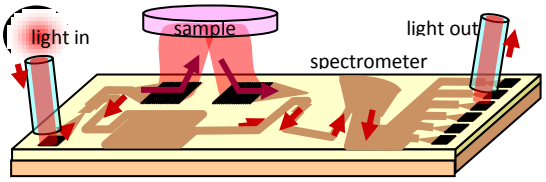

Figure 1. Nanophotonic circuit on SOI for FD-OCT.

A broadband light from a superluminescent diode is coupled to the photonic IC with a grating coupler and split into two arms via a splitter. The lower arm of the MZ acts as a reference wave, and in the upper arm, light is coupled out to the sample by a grating coupler. Another grating coupler collects the reflected light from the sample and couples it back to the waveguide leading to the combiner. A combiner at the other end of the MZ combines the reference and sample arm beams, and leads to a Planar Concave Grating (PCG) based spectrometer. The PCG spatially disperses the wavelength components and each component goes to an output waveguide. The beam from the output waveguides of the PCG are again collected by fibers from the grating couplers situated on the end points of the waveguides.

III Planar Concave Grating(PCG) Design

We used a Planar Concave Grating (PCG) based on Rowland geometry to form the spectrometer of the OCT. The channel spacing of the spectrometer defines the maximum achievable penetration depth, and its bandwidth determines the axial resolution. The resolution of the spectrometer scales linearly with the concave grating size [3].The design was limited to 3x6 mm area available on mask space, enabling 50 channels with 1nm channel spacing. The corresponding OCT parameters for this design

are 350µm measurement depth and 15 µm axial resolution.

IV Focusing Grating Coupler

Ideally, the light coupled out from the planar photonic integrated circuit should be focused on the sample to have a higher lateral resolution. However, the mask designs for the SOI platform had to be send in short period of time and planar gratings were used in the design for probing the sample and collecting the light reflected from the sample. Later, focusing grating couplers (FGC) have been investigated trough simulations as focusing elements. A FGC is a chirped and curved grating. The propagating light is progressively scattered by the etched grating and projects the light into the free space region above the waveguide surface and focuses it to a point. Fig.2 shows the simulated intensity profile of the light at the focal plane using a FGC with size 40x40µm and 350µm focal length.

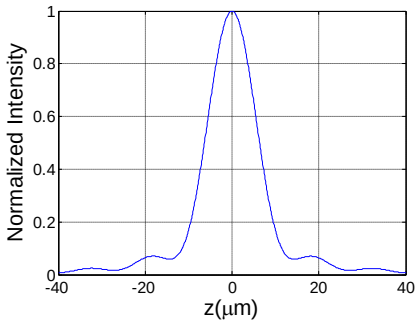

Fig.2 Intensity profile on the focus plane of a 40x40 µm FGC.

V Fabrication and Measurement

The designed photonic IC for FD-OCT is fabricated using CMOS fabrication technology adapted to photonics SOI. Fig.3 shows detailed scanning electron microscope (SEM) images of the PCG on the photonic IC.

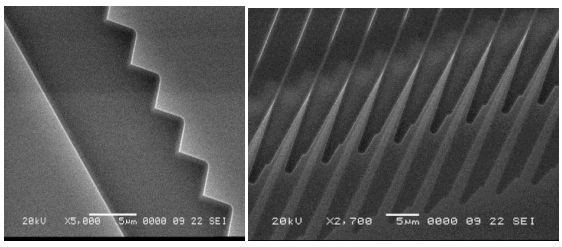

Fig.3 (a) grating teeth (b) output waveguide tapers of the PCG.

The fabricated chip is characterized. The measured spectral response of ten channels of the PCG is shown in Fig4.

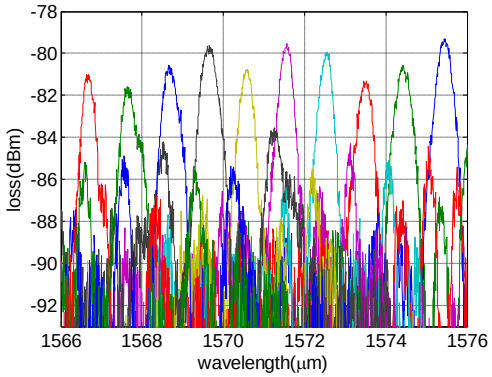

Fig.5 Spectral response of the first 10 channels of PCG.

The loss in the system is significantly larger than a fiber based OCT, 8 dB per grating coupler (x4), and 13 dB for the PCG. The total loss was on the same order of the sensitivity with the measurement system available in the lab, thus not enabling OCT measurements.

VI Conclusions

This study provided a better understanding of the challenges to implement a miniaturized FD-OCT on an SOI based photonic IC. Considering the losses, internal reflections, the detection scheme and the focusing out of the planar structure, FD-OCT can be realized as a photonics IC.

References

[1] R. A. Leitgeb et al. (2003) "Performance of Fourier Domain vs. Time Domain optical coherence tomography," Opt. Express 11, 889-894

[2] W. Bogaerts et al. (2006) "Compact Wavelength-Selective Functions in Silicon-on-Insulator Photonic Wires",J. Selected Topics in Quantum Electronics, 12(6), p.1394-1401

[3] J. Brouckaert et al. (2007), "Planar Concave Grating Demultiplexer Fabricated on a Nanophotonic Silicon-on-Insulator Platform," J. of Lightwave Technology, vol. 25, pp. 1053-1060.

Contents

Abbreviations

OCT Optical coherence tomography

TD-OCT Time Domanin optical coherence tomography

FD-OCT Fourier domain optical coherence tomography

MZ Mach-zehnder

SNR signal to noise ratio

SOI silicon on insulator

PCG planar concave grating

FSR free spectral range

LD linear dispersion

FPR free propagation region

SEM scanning electron microscope

ICP inductively coupled plasma

Chapter 1

Overview of Optical Coherence Tomography

Optical Coherence Tomography (OCT) is an imaging technique that is analogous to ultrasound imaging except that it uses light echoes rather than sound. It enables high speed, high resolution, cross-sectional imaging of internal structures in materials. Its potential for medical applications was first demonstrated by imaging in vitro human retina by Huang et al. in 1991[1]**.** Since then, significant contributions have been made to the development of this technology which significantly improved the imaging speed and quality. OCT has also benefited from advances in photonics technology during this period. The resolution and sensitivity of OCT systems have been improved as the current technology offers many possibilities for broadband sources and more sensitive photo detectors. The technology has matured and OCT is successfully commercialized especially in the ophthalmic sector where it currently generates sales in excess of £30m a year[2] .

There are two basic modalities of OCT: Time-Domain OCT (TD-OCT) and Fourier-Domain OCT (FD-OCT). These two modalities are briefly discussed in the section below. Extended treatment is given to FD-OCT as it is the subject of the thesis.

In the remaining sections, the specifications of OCT and requirements for integrated photonics OCT are elaborated. Following the literature review of OCT, the aim of the project and the organization of the thesis is presented.

1.1 Time Domain-Optical coherence tomography (TD-OCT)

Time Domain OCT (TD-OCT) is the initially developed form of OCT system. It is simply a low coherence Michelson interferometer with a movable reference mirror. The schematic shown in Figure 1.1 is a TD-OCT.

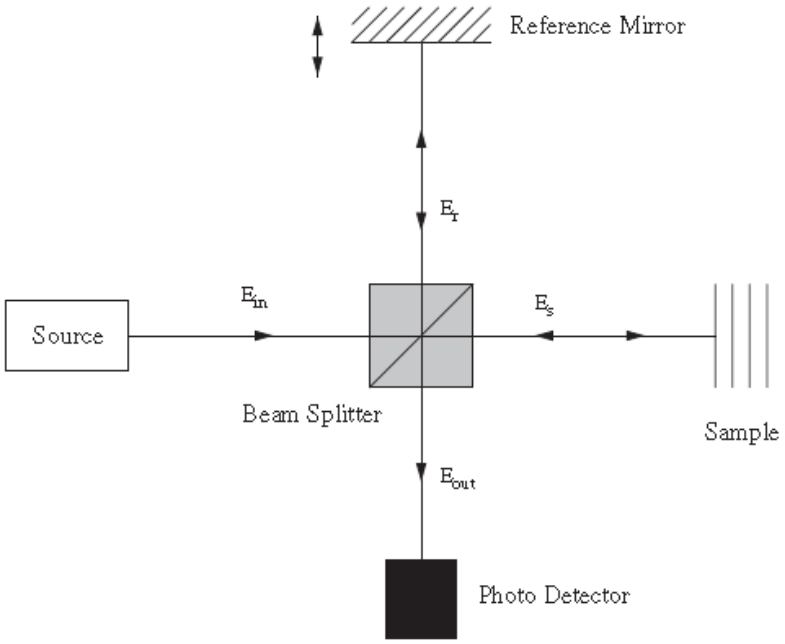

Figure 1.1: Basic OCT system based on Michelson interferometer

Light from a broadband source is incident on the beam splitter where it is split into two components, one half going to the reference mirror and the other half to the sample to be imaged. The reference arm beam reflects from the mirror and the sample arm beam undergoes multiple reflections from the layers within the sample. Upon reflection from the reference mirror and the sample, both light beams reunite and form an interference pattern. The photo detector records the interference pattern. Here, interference pattern will be detected only if the optical path difference between the reference arm and the sample arm light is within the coherence length of the light source. A well detailed mathematical explanation of the interference phenomenon of the OCT system is given by Fercher[3].

The intensity observed in the photo detector will be of the form:

$$I = I_r + I_s + 2I_s I_r \cos[\Delta\phi(\Delta z)] \qquad (1.1)$$

where $\Delta\phi$ is the phase accumulated in displacing the reference mirror by Δz, I_r and I_s are the intensities of the reference arm and the sample arm beams respectively[4].

As can be seen from the expression for the intensity, the first two terms are constant and the third term contains the reflectivity information from a certain depth of the sample. The reference mirror is displaced horizontally to make the depth scan. When the mirror is displaced, the optical path length of the reference arm beam changes so that it interferes with back scattered light from different depth levels of the sample. The signal from the detector is processed to extract its envelope which gives the reflectivity profile of the sample**.** This is called an axial scan or A-scan. In order to obtain 2D information, the beam or the sample is scanned in lateral direction and axial scans are combined together. This same information can also be obtained without a need for mechanical scan of the reference mirror by using the Fourier Domain Optical Coherence Tomography (FD-OCT).

1.2 Fourier Domain Optical Coherence Tomography

The FD-OCT system does not require moving the reference mirror to make a depth scan. Instead, information about the axial reflectivity profile is obtained by taking the inverse Fourier transform of the detected intensity spectrum[5]. This enhances the data acquisition rate of the OCT system, but requires a diffraction grating and an array of photodetectors forming a spectrometer to measure the spectrum of the interference. The basic scheme of an FD-OCT is given on fig.1.2.

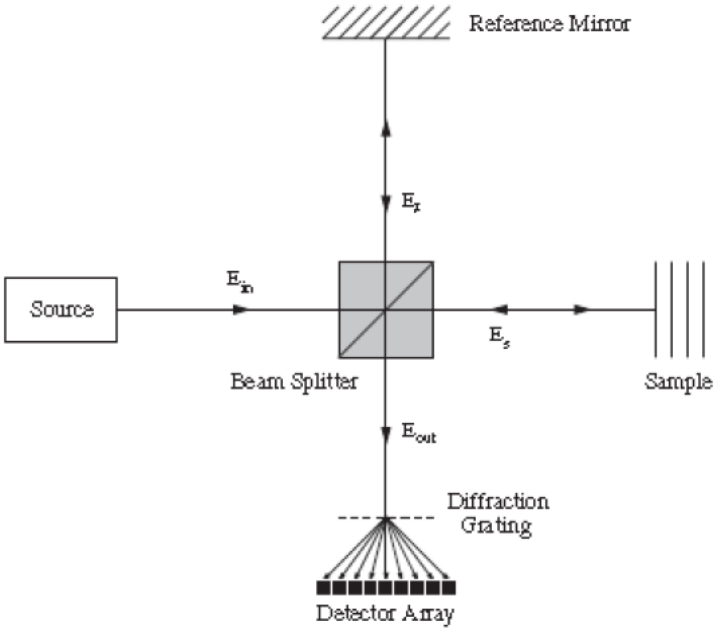

Figure 1.2: A schematics of Fourier Domain OCT system

The diffraction grating splits the output light field into corresponding wavelength components, leading each component to a specific detector of the detector array. The photocurrent $i(t)$ at the detector (a square law detector) is given by:

$$i(t) = \frac{\eta e}{h\nu} \frac{\langle |E_R + E_S|^2 \rangle}{2Z_o} \tag{1.2}$$

where η denotes the quantum efficiency of the detector, e denotes the electron charge, $h\nu$ denotes the photon energy, Z_o denotes the intrinsic impedance of free space, and the brackets denote averaging over the response time of the detection system.

Here, E_R and E_S are the electric field of the reference and the sample beams and take the forms:

$$E_R(\omega) = E_o(\omega) r_R \exp[i(2kL_R)] \tag{1.3}$$

$$E_S(\omega) = E_o(\omega) \exp[i(2kL_S)] \int_0^\infty r'_S(z) \exp[i(2n_S kz)]\, dz \tag{1.4}$$

where $E_o(\omega)$ refers to the electric field amplitude of the source, L_S & L_R are the two arm lengths of the interferometer, z is the distance from the equal path length plane to the back scatterers along the A-line in the sample to be imaged, and n_S is the average refractive index of the sample , k is the wavenumber in free space, $r'_S(z)$ is the apparent amplitude reflectivity density (reflectivity per unit depth) of the back scatterers along the A-line in the sample.

Apart from a constant scaling factor, the spectral interferogram is given by:

$$I(k) = |E_R(k) + E_S(k)|^2 \tag{1.5}$$

Substituting (1.3) & (1.4) in (1.5), we obtain

$$I(k) = S(k) r_R^2 + 2S(k) r_R \int_0^\infty r'_S(z) cos[2k(n_S z)]\, dz + S(k) \left| \int_0^\infty r'_S(z) exp[i2k(n_S z))]\, dz \right|^2 \tag{1.6}$$

where, $S(k) = |E_o(kc)|^2$ is the source power spectral density distribution. If we assume:

$$\hat{r}'_S(z) = \begin{cases} r'_S(z) & if\ z \geq 0, \\ r'_S(-z) & if\ z \leq 0. \end{cases}$$

The second term in (1.6) can be represented as a Fourier transform, and becomes

$$I(k) = S(k)\left\{r_R^2 + r_R\int_{-\infty}^{\infty}\hat{r}'_S(z)exp[i2k(n_S z))]dz + \frac{1}{4}\left|\int_{-\infty}^{\infty}\hat{r}'_S(z)exp[i2k(n_S z))]\,dz\right|^2\right\} \quad (1.7)$$

Changing the variable as $z = {z'}/{2n_S}$ (1.7) becomes

$$I(k) = S(k)\left\{r_R^2 + \frac{r_R}{2n_S}\mathcal{F}\left\{\hat{r}'_S\left(\frac{z'}{2n_S}\right)\right\}(k) + \frac{1}{16n_S^2}\left|\mathcal{F}\left\{\hat{r}'_S\left(\frac{z'}{2n_S}\right)\right\}\right|^2\right\} \quad (1.8)$$

Now, if we take the inverse Fourier transform of (1.8) we can recover the reflectivity profile of the sample.

$$\mathcal{F}^{-1}\{I(k)\}(z') = \mathcal{F}^{-1}\{S(k)\}(z') * \left\{\frac{r_R^2}{2n_S}\delta\left(\frac{z'}{2n_S}\right) + \frac{r_R}{2n_S}\hat{r}'_S\left(\frac{z'}{2n_S}\right) + \frac{1}{16n_S^2}@b\left\{\hat{r}'_S\left(\frac{z'}{2n_S}\right)\right\}\right\}$$

Here, * denotes convolution, and @{} denotes the autocorrelation-function operator.

With a change of variable by $z' = 2n_S z$ and using the Wiener-Khinchin theorem[6], the above equation becomes:

$$\mathcal{F}^{-1}\{I(k)\}(2n_S z) =$$
$$\mathcal{F}^{-1}\{S(k)\}(2n_S z) * \left\{\frac{r_R^2}{2n_S}\delta\left(\frac{z'}{2n_S}\right) + \frac{\boldsymbol{r_R}}{\boldsymbol{2n_S}}\hat{\boldsymbol{r}}'_{\boldsymbol{S}}(\boldsymbol{z'}) + \frac{1}{16n_S^2}@\{\hat{r}'_S(z')\}\right\} \quad (1.9)$$

The second term in the braces is the A-line image$\hat{r}'_S(z)$. The first and last terms, however, represent spurious images. The first term is a DC term, and the third term is in general negligible for weakly scattering media such as biological tissue.

To recover the true image, one may take another interferogram with kz' shifted by π, which causes a sign change in (1.9):

$$I_2(k) = S(k)\left\{r_R^2 - \frac{r_R}{2n_S}\mathcal{F}\left\{\hat{r}'_S\left(\frac{z'}{2n_S}\right)\right\}(k) + \frac{1}{16n_S^2}\left|\mathcal{F}\left\{\hat{r}'_S\left(\frac{z'}{2n_S}\right)\right\}\right|^2\right\} \quad (1.10)$$

Taking the difference between (1.7) and (1.10) yields

$$\Delta I(k) = S(k)\frac{r_R}{n_S}\mathcal{F}\left\{\hat{r}'_S\left(\frac{z'}{2n_S}\right)\right\}(k) \qquad (1.11)$$

where $\Delta I(k) = I(k) - I_2(k)$. The A-line image can be recovered by

$$\hat{r}'_S\left(\frac{L'_S}{2n_S}\right) = \frac{n_S}{n_R}\mathcal{F}^{-1}\left\{\frac{\Delta I(k)}{S(k)}\right\}(z') \qquad (1.12)$$

Changing the variable by $z' = 2n_S z$ leads to

$$\hat{r}'_S(z) = \frac{n_S}{n_R}\mathcal{F}^{-1}\left\{\frac{\Delta I(k)}{S(k)}\right\}(2n_S z) \qquad (1.13)$$

This equation shows that the subtracted and deconvolved spectral interferogram in the braces recovers an ideal image; the deconvolution involves simply dividing $\Delta I(k)$ by $S(k)$. Although deconvolution can sharpen the image, one should exercise caution in the presence of noise.[7]

1.3 Design issues of OCT system

The specifications of optical coherence tomography systems vary widely according to their design and data acquisition speed requirements of the tissue to be imaged. The most important specifications of an OCT system are: measurement range, resolution (axial and lateral), penetration depth, and sensitivity.

1.3.1. Measurement range

The measurement range of the FD-OCT system depends on the spectral resolution of the spectrometer. Practically the useful information about the object structure is obtained by the Fourier transform of the sampled spectrum. If $\Delta\lambda$ width of the spectrum illuminates *N* pixels of the line CCD detector, then based on Nyquist sampling criteria the maximum path difference that can be measured by a FD-OCT system is given by[8]

$$l_{max} = \frac{1}{4n}\frac{\lambda_o^2}{\Delta\lambda}N = \frac{1}{4n}\frac{\lambda_o^2}{\delta\lambda} \qquad (1.14)$$

where δλ is the wavelength resolution of the spectrometer. For example, a spectrometer having a wavelength resolution of 0.1nm, can give a measurement range as deep as 4mm for a source of center wavelength *1550nm*.

1.3.2 Axial resolution

The axial resolution of an OCT system is a characteristics of the source used. It is defined as half of the coherence length of the light source l_c. Assuming a light source having a Gaussian spectrum, the coherence length is given as:

$$l_c = \frac{4\ln(2)}{\pi}\frac{\lambda_o^2}{\Delta\lambda} \approx 0.88\frac{\lambda_o^2}{\Delta\lambda} \qquad (1.15)$$

Where λ_o is the source centre wavelength, and $\Delta\lambda$ is the FWHM spectral bandwidth. Therefore, the OCT axial resolution R_{OCT} becomes: [5]

$$R_{OCT} = \frac{1}{n_s}\frac{l_c}{2} \approx \frac{0.44}{n_s}\frac{\lambda_o^2}{\Delta\lambda} \qquad (1.16)$$

where n_s represents average refractive index of the sample.

As the source dictates the possible axial resolution of the OCT system, choosing appropriate source is important issue in the design of OCT system. Most commonly used broadband sources are super luminescence diodes (SLDs). People demonstrated axial resolution of $3\mu m$ in air by using two SLDs conjugated together.[9] Another potential light source is a supercontinuum source generated by nonlinear processes from a femtosecond Titanium Sapphire laser, which can provide an OCT system an axial resolution in sub micrometer scale.[10] For example, a *50nm* bandwidth source with center wavelength *1550nm* can give axial resolution around $15\mu m$.

1.3.3 Lateral Resolution

The lateral resolution in OCT is limited by the size of the probe beam diameter. The lateral resolution imposed by the probing optics of the system is a consequence of the Abbe's rule which is given as: [11]

$$\Delta x = 1.22 \frac{\lambda}{2(\mathrm{NA})} \qquad (1.17)$$

where *NA* is the numerical aperture of the microscope objective.

The very advantage of OCT over other optical imaging devices is that the lateral resolution is completely independent of the axial resolution which enables system designers to optimize the axial and lateral resolutions separately. However, the lateral resolution is related to the depth of focus. This limits the depth range over which lateral resolution does not degrade significantly.

This depth of focus is determined by the source wavelength and numerical aperture of the probing optics. It is given by the expression:[3]

$$DOF = 2 \frac{\lambda n_s}{(NA)^2} \qquad (1.18)$$

where $n_s$is the average refractive index of the sample, λ the center wavelength of the broadband source, and *NA* corresponds to the objective of the scanning probe and determines the spot size of the sample beam.

Physically, the spot size of the beam is a direct consequence of the scattering nature of the sample to be imaged. If the tissue to be imaged is of high scattering nature, the *NA* necessary to capture the reflected light should be fairly large and hence negatively influencing the depth of focus. That is why the relatively small penetration depth of OCT system limits its application for imaging highly scattering tissue. Reported penetration depths are between 1 and 3 mm, depending on the opacity of the tissue, such as skin, and the wavelength of light used.[3]

1.3.4 Sensitivity/ dynamic range

Sensitivity of an OCT system is related to the source and detectors of the system. It is the minimum power the receiver needs for error free detection. The optical signal received by the receiver is mixed with background noises of which the most significant are: shot noise, excessive intensity noise, and thermal noise. So, there exists a threshold value of incident power signal below which the receiver gives erroneous result. It is simply quantified as the optical power signal to noise ratio SNR. Rigorous formulation of the sensitivity using optical communication

theory is given in the work of Fercher[5]. But the sensitivity takes pretty short expression for the case of shot noise limited intermediate signal power:

$$SNR = \frac{1}{4}\frac{\eta}{h\nu}\frac{P_{source}}{B} \qquad (1.19)$$

where η is the quantum efficiency of the photodetector, h Planck's constant, and ν, P_{source} & B are frequency, optical power of the source and the electronics bandwidth. The above expression implies that the sensitivity of a shot noise dependent OCT system varies proportional to the source power and inversely to the electronic bandwidth. In practice it is not possible to indefinitely improve the sensitivity by increasing the source power (even if the technology affords high power source), because the tissue to be imaged has some maximum permissible exposure levels.

In the case of FD-OCT, the SNR scales linearly as the number of detectors used, M.

$$SNR = M\frac{1}{4}\frac{\eta}{h\nu}\frac{P_{source}}{B} \qquad (1.20)$$

Which implies that FD-OCT is much more sensitive than TD-OCT. Signal to noise ratio studies have shown that Fourier domain OCT provides signal to noise ratio that is more than 20 dB better than conventional TD-OCT.[12]

1.3.5 Effect of pixel width of spectrometer on OCT signal

The spectrum measured with a spectrometer can be approximated by a convolution of the response function *R(k)* of the spectrometer and the true intensity spectrum, so that the intensity in the detector plane in *k* space is $R(k)\otimes I(k)$,where *k* is the wavenumber. *R(k)* depends on the spectrometer characteristics, such as focal length, diffraction grating, and entrance-slit width.

Since the spectrometer has a finite pixel width, the convolved light intensity in the detector plane is then integrated over the pixel area, yielding the following expression for the signal S_i, collected on a given pixel at position x_i:

$$S_i = \int_{x_i - a/2}^{x_i + a/2} R(k) \otimes I(k) dk \qquad (21)$$
$$= \int_{-\infty}^{\infty} rect(k - k_i)\{R(k) \otimes I(k)\}\, dk$$
$$= \{rect(k) \otimes R(k) \otimes I(k)\}(k_i)$$

where a is the pixel width, $rect(k)$ is a rectangle function with unit amplitude for $|k| < a/2$ and zero elsewhere. The general form of the signal S can be represented as function of k as:

$$S(k) = \Pi(k)\{rect(k) \otimes R(k) \otimes I(k)\} \qquad (22)$$

where $\Pi(k)$ is a Dirac comb of period δk, the pixel spacing.

Axial image is obtained by taking the Fourier transform of this signal, and the reflection profile of the sample is given by

$$S(k) = \Pi(z) \otimes \{P(z)R(z)\mathcal{F}^{-1}(I(k))\} \qquad (23)$$

P(z) is a sinc function and *R(z)* is in general a Gaussian function, thus both pixel width and spectrometer resolution affect the spectral intensity as low pass filters[13] . A more detail analysis of the combined effect of pixel width and spectrometer resolution on OCT image is given in Chapter 2.

1.4 Implementation of FD-OCT on nanophotonic circuit

There have been significant developments in the technology of photonic integrated circuits. Research is going on optimizing material systems that can allow considerable integration of photonic circuits. Silicon-on-Insulator (SOI) is perceived to be a promising material system to push the integration density of photonic circuits. The high index contrast of Silicon with insulator (or air) allows strong confinement of light by subwavelength scale nanophotonic components. The low loss of silicon in the communication wavelength range is

another advantage. Above all, the compatibility of this platform with the well established wafer scale CMOS technology gives a great economical and technological advantage.

The Photonics research group in the INTEC department of Ghent University has a well established SOI research platform. This group has demonstrated the fabrication of different nanophotonic components on SOI[14 15 16 17 18 19]. The drive to start the implementation of OCT on integrated photonic circuit has come from the availability of these nanophotonic components and the research experience of the group. Although not optimized for OCT, all of the necessary components required for an OCT system set up, input/output grating couplers, y-splitters and combiners, nanophotonic wires, adiabatic tapers, and waveguides are available. For the spectrometer, the group has demonstrated a Planar Concave Grating (PCG) which has 4 output channels with a channel spacing of $20\mu m$[19]. Very recently, it has been optimized to 30 channels with *3.1nm* channel spacing (personal communication).

1.5 Aim of the thesis

The main aim of this project lies on exploring the SOI platform for OCT application. One great challenge is that the PCG demonstrated doesn't have the required wavelength resolution. Our OCT needs at least *1nm* wavelength resolution to get tissue image as deep as $350\mu m$. So, in this work we try to extend the PCG resolution to *1nm*. In addition, the bandwidth of the PCG is small which limits the axial resolution. We also made an effort to increase the output channels of the PCG to *50*, hence resulting in a bandwidth of *50nm*.

Another important component of the OCT system is the probing optics. In free space optics, the probing system consists of a set of optimized lenses and mirrors which are widely available as commercial, off-the-shelf components. But, it is difficult to implement achromatic lenses and mirrors on an integrated photonics chip. We studied the potential of a chirped and curved grating coupler called Focusing Grating Coupler (FGC) for forming the probing component of the OCT system.

Using these inputs we proposed an onchip OCT with a Mach-Zehnder (MZ) interferometer configuration. The photonic circuit is shown in figure 1.3.

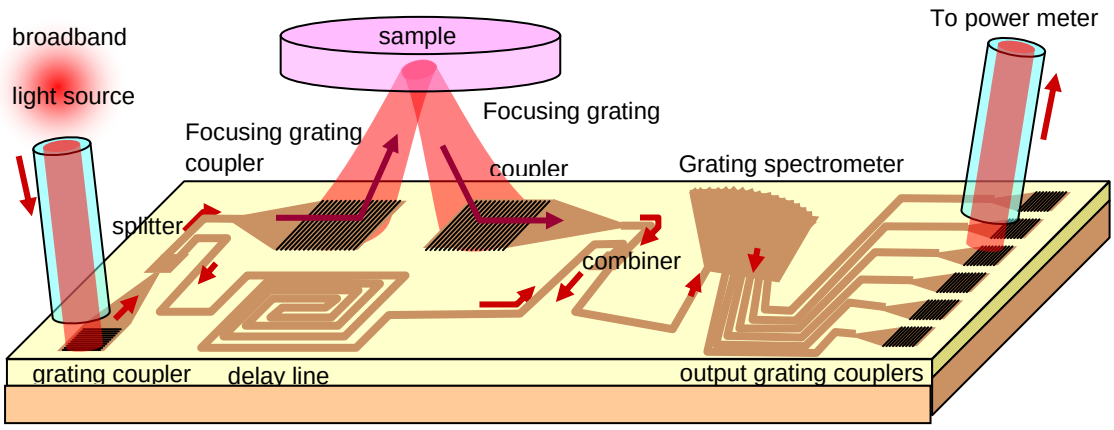

Figure 1.3: Schematic of Fourier Domain OCT photonic IC.

A broadband light at 1550nm from a superluminescent diode is coupled to the photonic IC with a grating coupler and split into two arms via a splitter. The lower arm of the MZ acts as a reference wave, and in the upper arm, light is coupled out and focused to the sample by a focusing grating coupler (FGC). A modified FGC collects the reflected light from the sample and couples it back to the waveguide leading to the combiner. A combiner at the other end of the MZ combines the reference and sample arm beams. The configuration uses a Planar Concave Grating (PCG) as a spectrometer of the detection system[19]. The light from the combiner goes to the input waveguide of the PCG, the PCG spatially disperses the wavelength components and each component goes to an output waveguide. The beam from the output waveguides is again collected serially by a fiber from the grating couplers situated on the end points of the output waveguides.

Chapter 2

Design and simulation of Planar Concave Grating Spectrometer

Planar Concave Gratings (PCGs) have been widely used in integrated optics. They have got applications in WDM systems as demultiplexers, in multi-wavelength lasers as external cavities, and as sensor elements in integrated optical spectrum analyzers[20]. This chapter discusses the theory and design issues of the PCGs. The first section introduces the basics of PCGs and their related design issues. Then, we discuss a model to calculate the performance of the PCG. Finally the simulation results are presented.

2.1 Theory of PCG

A concave grating is a periodic structure with the locus of the grating facet centers lying on a circle, and hence the name concave. Due to their curved geometry, the PCG not only spatially resolves wavelength components of an input light, but also it focuses them to a point. There are several configurations to implement the PCG. The most widely used approach is the Rowland circle geometry[21] [22]. Some people have showed other possible configurations like a recursive procedure to generate the grating facets profile[23]. In our design, we used the Rowland approach. This approach is discussed in detail by Chowdhury et al.[24]. The schematic diagram of the classical Rowland PCG is shown in figure 2.1.

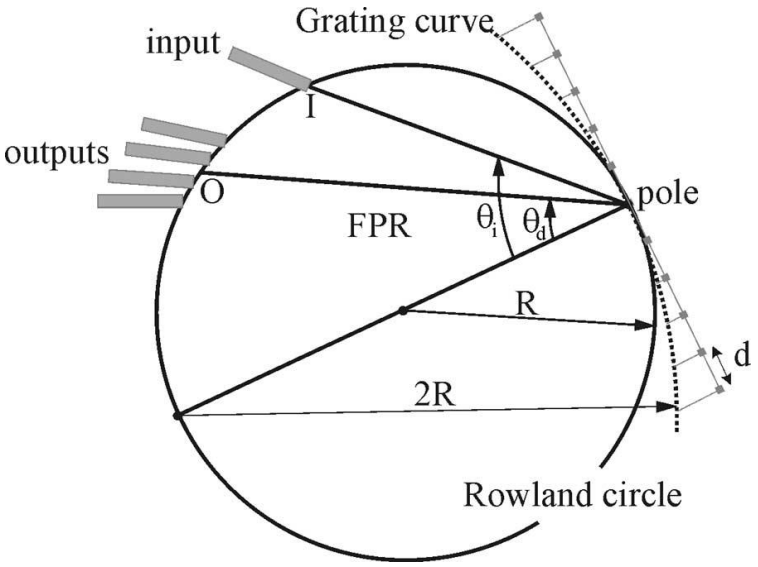

Figure 2.1: Schematics of the Rowland based Planar Concave Grating

In this geometry, the input and output waveguides end on a circle called the Rowland circle that has a radius of R. The centers of the grating facets lie on a circle that has a radius of 2R and tangent to the Rowland circle at a point called the pole of the grating. The pole is also the geometrical center of the grating. The projection of the grating facets centers on the tangent line are equidistance, and this distance is termed as the grating period, d.

According to the Rowland theory, in such configurations, light emanating from a point source A on the Rowland circle will be focused to another point B lying on the same circle. However, this is true only to a first approximation[23].

The condition for constructive interference for diffracted beams from adjacent facets is:

$$d(sin\theta_i + sin\theta_d) = m\frac{\lambda}{n_{eff}} \qquad (2.1)$$

where d is the grating period, and θ_i and θ_d are the angles the incident beam and the diffracted beam make with the Rowland circle diameter passing through the pole, respectively, m is a whole number which is called the order of diffraction, and λ is the free space wavelength, while n_{eff} is the effective index of the slab mode of the free propagation region.

2.2 Design of the PCG

The main specifications of the PCG are the wavelength resolution, number of output channels, operating wavelengths (bandwidth), and insertion losses. Other parameters which depend on these specifications are the Linear Dispersion (LD), and the Free Spectral Range (FSR).

The Linear Dispersion (LD) defines the extent to which a spectral interval is spread out across the focal field of the spectrometer and is expressed in nm/mm. In other terms, it is the ratio of the separation of the output waveguides to the channel spacing. It quantifies the PCG's ability to resolve fine spectral details.[25]

It is given by the equation:

$$LD = \frac{2R}{cos\theta_d}\frac{m}{d}\frac{n_g}{n_{eff}^2} = \frac{2R}{\lambda}\frac{(sin\theta_i + sin\theta_d)}{cos\theta_d}\frac{n_g}{n_{eff}} \qquad (2.2)$$

where

$$n_g = n_{eff} - \lambda\left(\frac{dn_{eff}}{d\lambda}\right) \qquad (2.3)$$

is the group index of the Free Propagation Region (FPR) slab mode. Detail proof of this expression is given in Chowdhury et al [24]. As shown in (2.2), the LD is a direct function of the grating size. Thus, high resolution PCG demands large grating size.

The width of the output waveguides is chosen to be $2.25\mu m$. The spacing between the waveguides is $2.0\mu m$.This choice is made in such a way that the waveguides are not close enough to allow mode coupling between them. Thus, the LD of our PCG is around$5.5\mu m/nm$. We could have gone to a much lower channel spacing (and hence high LD), but the size of the PCG will be considerably large. And we are constrained to a smaller chip size due to economical reasons.

The Free spectral range is a band of wavelength where the PCG can operate without the overlapping of the diffracted wavelengths for consecutive orders. It is given by the expression:

$$FSR = \frac{\lambda}{m}\left[1 - \frac{m+1}{m}(1 - \frac{n_g}{n_{eff}})\right]^{-1} \qquad (2.4)$$

It can be derived from the grating equation by requiring the diffraction angle for the beam of wavelength λ in an order *(m+1)* to be the same as that of a beam with wavelength $(\lambda + d\lambda)$ diffracted in a lower order *m*. The required Free Spectral Range (FSR) determines the selection of the diffraction order of the grating. In our case a FSR of *115nm* is assumed which gives *10* to be the order of diffraction.

The bandwidth of our SLD source is around 50nm; this choice is made in line with the axial resolution requirement of the OCT system. Thus, the operating wavelength range of the PCG is between $1.530\mu m$ & $1.580\mu m$, with the central wavelength being $1.55\mu m$.

The channel spacing requirement is determined by the sought measurement range of the OCT device. Figure 2.2 below shows the variation of measurement depth with channel spacing. We have assumed a $300\mu m$ measurement depth which translates to a $1nm$ channel spacing requirement of the PCG.

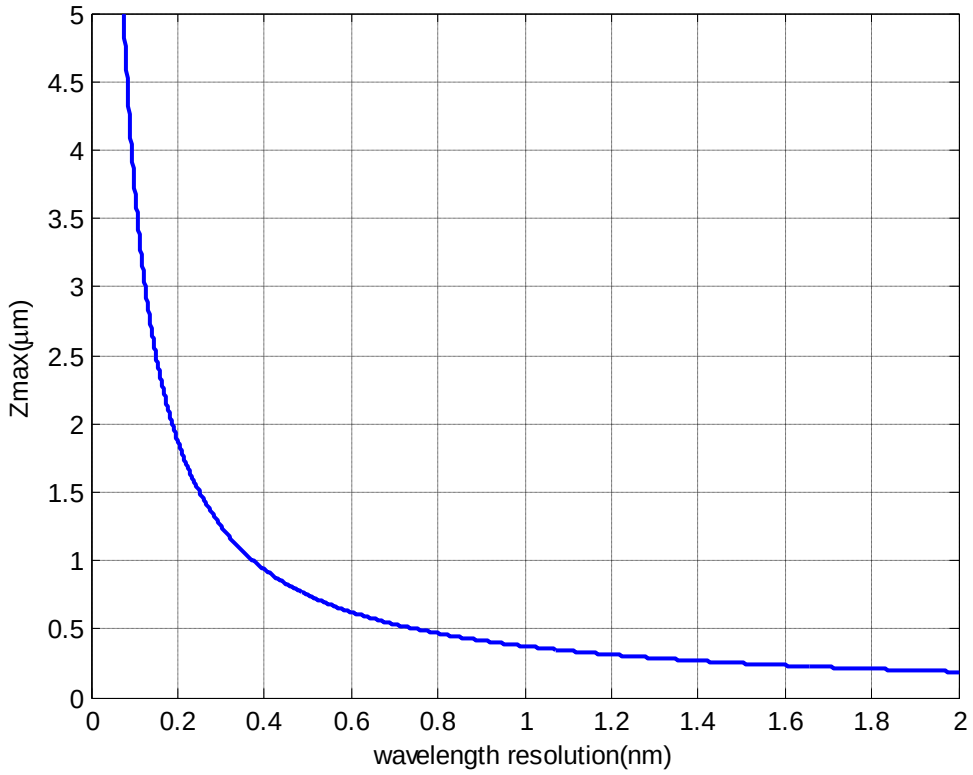

Figure 2.2: The effect of wavelength resolution of a spectrometer on maximum imaging depth of an OCT device without aliasing.

2.3 Simulation and modeling of the PGC

We used the scalar diffraction theory to simulate the performance of the PCG.[26] The schematic view of the grating along with the coordinate system used is shown in figure 2.3.

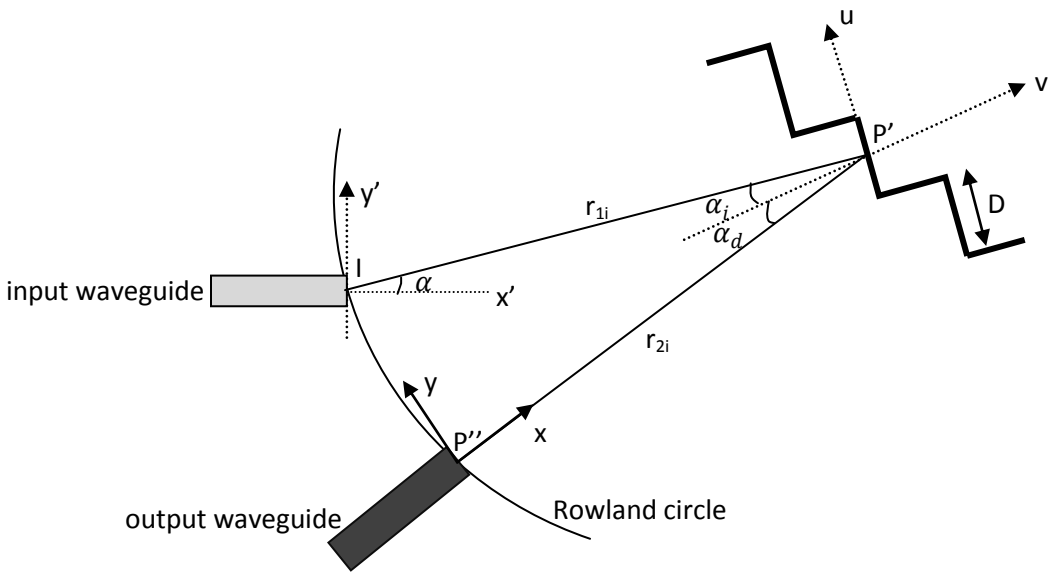

Figure 2.3: Schematic view of a concave grating and the coordinate systems used in the calculations.

Let P' be the center of the *ith* facet, and r_{1i} and r_{2i} represent the distance of the facet center from the input and output waveguides respectively.

The electric field profile of the TE polarized fundamental mode of the input waveguide is:

$$E_{input}\,(y') = E_o exp\left(-\frac{y'^2}{w_o^2}\right) \qquad (2.5)$$

where E_o is the amplitude, and w_o is the mode width. This gives the electric field at the input point I.

According to Kirchhoff-Huygens diffraction formula, the electric field incident at the center point of the i^{th} grating facet P' takes the form:

$$E_{inc,i}(u=0) = \frac{1}{2}\sqrt{\frac{n_{eff}}{\lambda}} \int_{input\ wg} E_{input,wg}(y') \frac{e^{-jkr_{1i}}}{\sqrt{r_{1i}}} (1+cos\alpha) dy' \qquad (2.6)$$

where $k = 2\pi n_{eff}/\lambda$ is the wavenumber within the slab waveguide. And the integral is done over the width of the input waveguide.

The diffracted field from the grating facet at point P'' on the Rowland circle then becomes:

$$E_{out,i}(y) = \eta\sqrt{\frac{n_{eff}}{\lambda}} \int_{-D/2}^{+D/2} E_{inc,i}(u) \frac{e^{-jkr_{2i}}}{\sqrt{r_{2i}}} \frac{[\cos(\alpha_i) + \cos(\alpha_d)]}{2} du \qquad (2.7)$$

Here α_i is the angle between the facet normal and the light incident on the facet, and α_d is the angle between the facet normal and the light reflected from the facet, *D* is the effective facet width, which in general varies across the grating, and η is the reflection coefficient of the facet. And $E_{inc,i}(u)$ is the field at point *u* on the grating facet.

The size of the grating facet is small compared to its distance from the input point, and thus the incidence angle α_i is generally small. This helps to make further simplification to the above formula. We do so by approximating the field incident on the grating facet to have constant amplitude, but linearly changing phase along the facet length as:

$$E_{inc}(u) = E_{inc}(u'=0) e^{+jkusin(\alpha_i)} \qquad (2.8)$$

Thus, (2.7) reduces to:

$$E_{out,i}(y) = \eta\sqrt{\frac{n_{eff}}{\lambda}} \int_{-D/2}^{+D/2} E_{inc,i}(u=0) e^{+jkusin(\alpha_i)} \frac{e^{-jkr_{2i}}}{\sqrt{r_{2i}}} \frac{[\cos(\alpha_i) + \cos(\alpha_d)]}{2} du \qquad (2.9)$$

The total field at point P'' is the superposition of the field diffracted from all the grating facets, and can be written as:

$$E_{out} = \sum_i E_{out,i} \qquad (2.10)$$

Having calculated the electric field profile on the output waveguide, the spectral response of the channel can be obtained by taking the overlap integral between this diffracted field E_{out} and the field profile of the fundamental mode of the output waveguide. In our design we used a $2.25\mu m$ wide output waveguides, obviously this supports other higher order modes. But, these modes are filtered out as the waveguides are adiabatically tapered to the *500nm*-wide single mode photonic wires.

2.4 Simulation results

To get spectral response of the PCG, the point where an input ridge waveguide meets the slab waveguide is chosen as an input point, and the point where an output ridge waveguides meets the slab waveguide is chosen as an output point. By changing wavelength in a certain range around the center wavelength and calculating the overlap integral with the output waveguide single mode profile, the spectral responses of the demultiplexer are obtained. The design parameters used for this simulation are summarized in table 2.1.

Parameter	Value	Parameter	Value
Number of grating facets	601	Number of channels	50
Period, d	4.27um	Channel spacing	1nm
Angle of incidence	41	Waveguide spacing	5.5um
Angle of diffraction	38.8	Linear dispersion	5.5um/nm
Order of diffraction	10	Free spectral range	117.14
Radius of the Rowland circle	3.95mm	Bandwidth	50nm
Output waveguide width	2.25um	Effective index	2.833
Overall size	4.89mmX2.04mm	Group index variation	-0.57/um
Output waveguide width	2.25um	Spacing b/n output waveguides	2.0um

Table 2.1: Parameters used in the simulation of the PCG

Figure 2.4 shows the spectral response of the middle two channels of the PCG. The loss is below *0.5dB*, however, the simulation doesn't consider the waveguide loss and other related losses, so the actual device can have a larger loss. The cross talk is below *60dB*.

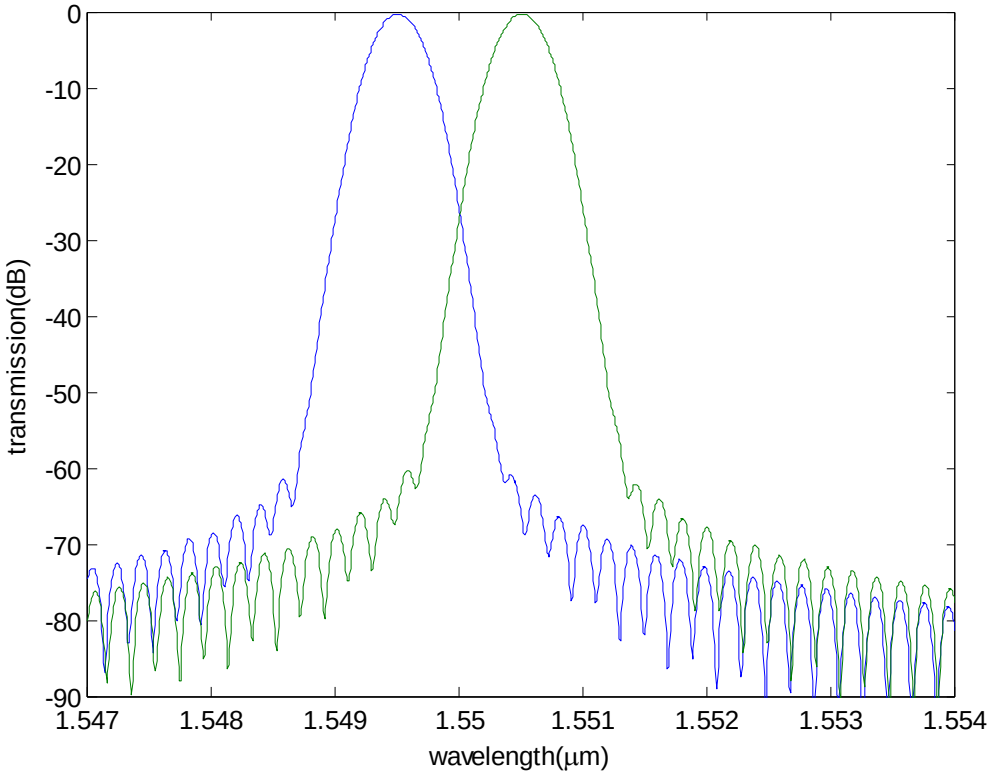

Figure 2.4: Spectral response of the PCG for the middle two channel channels.

The spectral response of the other channels is given in figure 2.5. As can be seen, the loss increases as one goes away from the central channel. Likewise, the crosstalk gets worse.

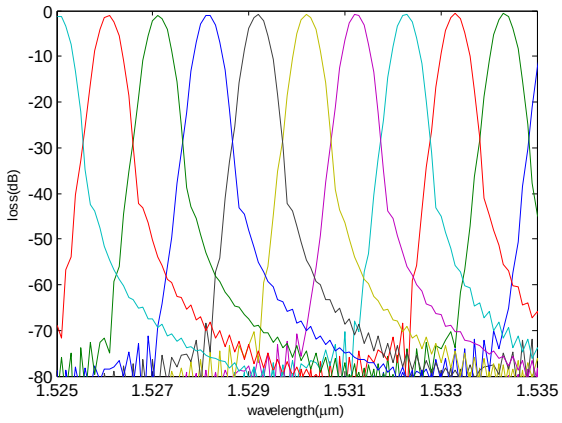

(a)

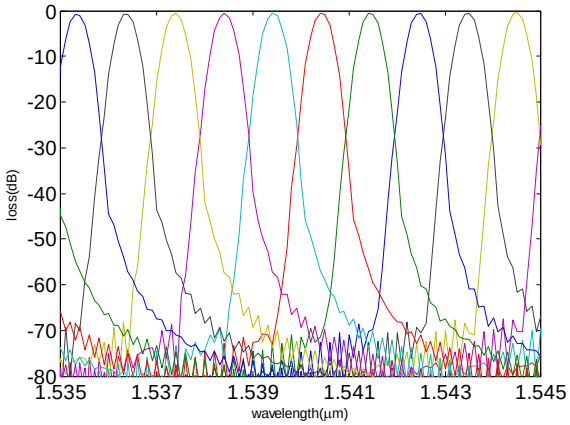

(b)

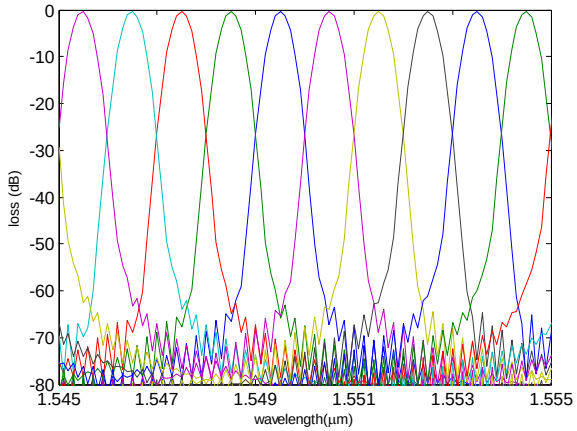

(c)

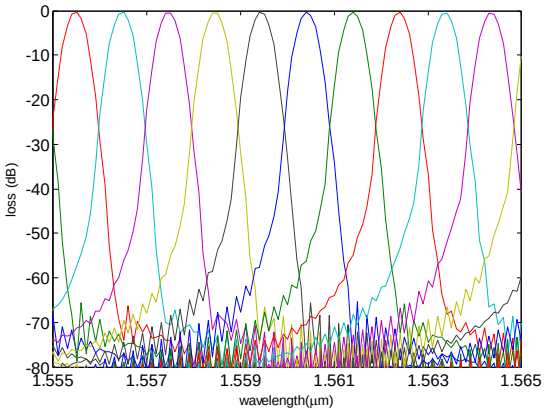

(d)

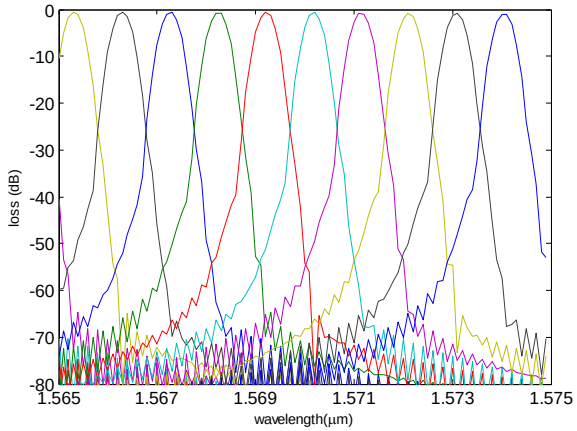

(e)

Figure 2.5: Spectral response of the PCG for the (a) first, (b) second (c) middle (d) fourth and (e) last 10 output channels .

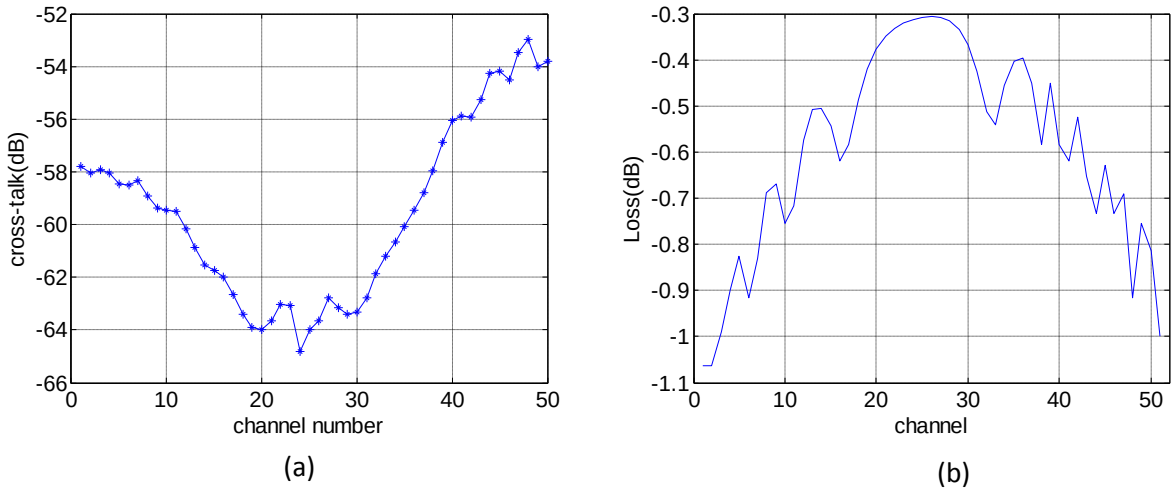

Figure 2.6: Cross-talk (a) and loss variation (b) along the output waveguides

Figure 2.6 (a) shows the variation of the crosstalk across the channels. The cross talk is minimum in the middle channels and gets worse as one goes away from the central channel. In average the cross-talk variation is about 0.34dB per channel. There is also asymmetry in the cross talk variation, this can be due to the fact that the output waveguides are not symmetrical with respect to the input waveguide. The loss variation about the central channel is also shown in figure 2.6(b). Like the cross talk, the PCG has minimum loss for the middle output channels. The overall average loss variation is around 0.028dB per channel.

2.5 Effect of the spectral response of the PCG spectrometer on OCT image

Based on the spectrometer simulation result, we have made analysis of the PCG spectral response effect on the OCT image. For the calculation, the analysis given in section (1.3.5) is used. The spectrometer affects the intensity spectrum as a low pass filter. The transfer function of the low pass filter is shown in figure 2.7.

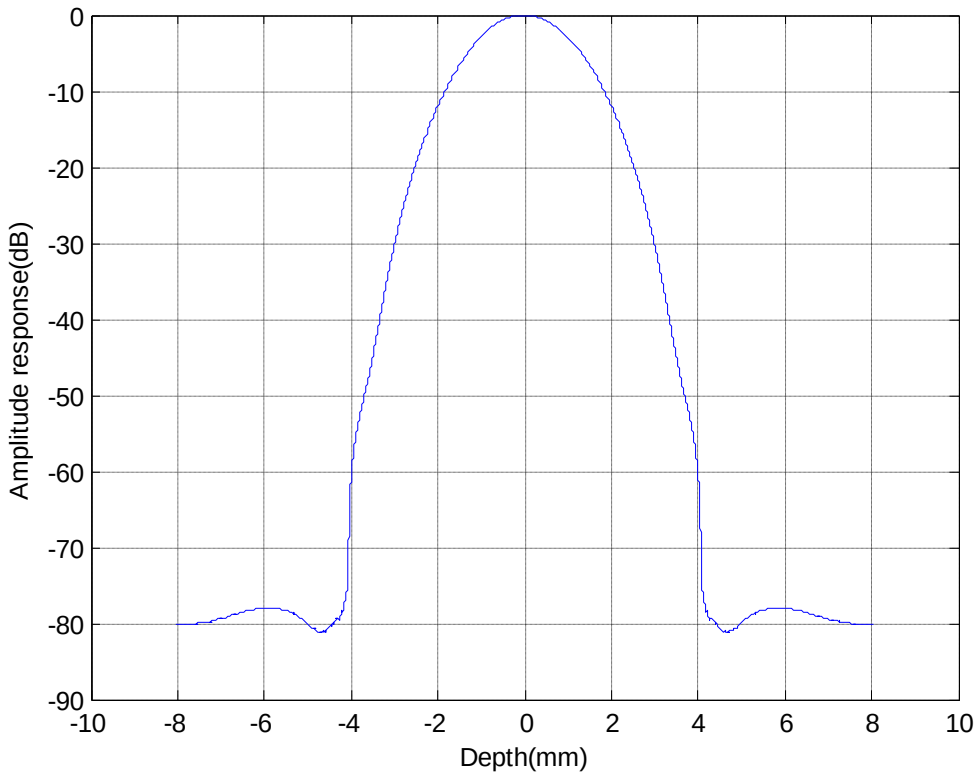

Figure 2.7: The spectrometer pixel width acts as a low pass filter for the intensity spectrum.

With a 10dB loss, the spectrometer can allow imaging as deep as 2 mm. Our OCT system is designed to give a maximum imaging depth of 350um, thus the loss encountered by the low pass filter is less than 2dB.

Chapter 3

Design and Simulation of Focusing Grating Coupler

In this chapter we explore the potential application of Focusing Grating Coupler as illuminating element of the integrated OCT system. First, an overview of fundamental principles of focusing grating couplers and their design issues are discussed. Then, the modeling of the interaction of light with a focusing grating coupler is explained. Finally, simulation results and the corresponding optimized design parameters are presented.

3.1.1 Theory of Focusing Grating Coupler

An important application of gratings is their use as an input/output coupler from a waveguide. A one dimensional uniform grating has been used extensively as a means to couple light out of a waveguide to a fiber.[27] When such one dimensional gratings are chirped, it helps to focus the output coupled wave to a line. Adding curvature to these chirped lines will focus the outcoupled light to a point. [28] Such a curved and chirped grating is called focusing grating coupler. Thus the focusing grating coupler not only does coupling out light, but also converts the input beam wavefront into a spherical wavefront.

A focusing grating coupler (FGC) can be employed as a focusing component of an integrated OCT system. The geometry of the focusing grating coupler is shown on figure 3.1. The figure shows a waveguide cross section with light travelling along the waveguide in the direction of the arrow on the left.

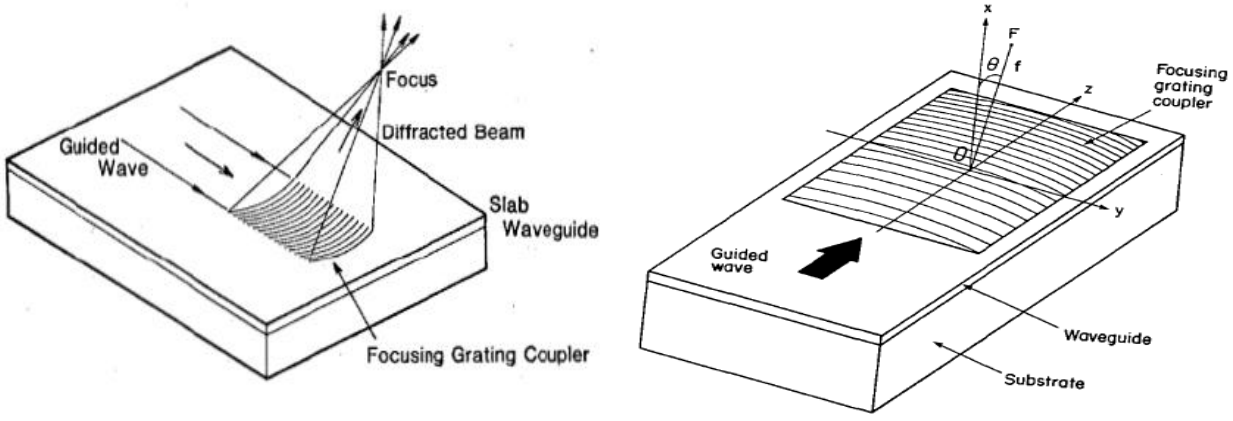

Figure 3.1: A focusing grating coupler configuration

The propagating light is progressively scattered by the etched grating and projects the light into the free space region above the waveguide surface and focuses it to a point. The FGC is generally used in integrated optic devices like optical disk pickups, [29] scanning optical microscopes[30], and interferometer position sensors.[31]

The pattern of the FGC is determined from the phase difference of the input guided wave and the expected outcoupled wave. The phase difference at a point *(x,y,z)* on the grating surface takes the form:

$$\Delta\Phi(x,y,z) = k_o n_{eff} z + k_o\sqrt{y^2 + (z - fsin(\theta))^2 + (fcos(\theta))^2} \quad (3.1)$$

$$\Delta\Phi = 2m\pi + constant \quad (3.2)$$

where k_o is the wavevector in free space, n_{eff} is the effective mode index of the waveguide, *f* is the distance of the focal point from the origin, and m is the number of the grating line.
Thus, the equation that gives the loci of the grating pattern lines becomes:

$$n_{eff} z + \sqrt{y^2 + (z - fsin(\theta))^2 + (fcos(\theta))^2} = m\lambda \quad (3.3)$$

This equation can be reduced to the standard form of a hyperbolic equation as:

$$\left[z - \frac{m\lambda n_{eff} - fsin(\theta)}{n_{eff}^2 - 1}\right]^2 - \frac{y^2}{(n_{eff}^2 - 1)} = \frac{(n_{eff}^2 - 1)(f^2 - m^2\lambda^2) - \left[fsin(\theta) - m\lambda n_{eff}\right]^2}{(n_{eff}^2 - 1)^2}$$

This shows that the locus of the m^{th} grating line is a hyperbola with eccentricity

$$e = \sqrt{1 + (n_{eff}^2 - 1)^2}$$

and center at

$$(0,0,\frac{m\lambda n_{eff} - fsin(\theta)}{n_{eff}^2 - 1})$$

3.1.2 Design Issues of FGC

Since an FGC performs the functions of both an in/out coupler and a lens simultaneously, its performances as a coupler and as a focusing lens are described with the coupling efficiency and the focusing performance, respectively. Besides these, the chromatic aberration of the FGC is a property that has to be taken into account especially if one is working with broadband sources. Some of the important parameters which determine such properties are grating size, filling factor, etching depth, etc.

The size of the FGC is determined by considering Gaussian optics of an equivalent lens system. The focus spot width, which corresponds to the beam waist of a Gaussian should be equivalent to the sought transverse resolution of the OCT system. Roughly, a $20\mu m$ transverse resolution is assumed. The corresponding Rayleigh length becomes $200\mu m$. This will allow an imaging depth of $400\mu m$ without a significant loss of lateral resolution. Based on this argument, the focal length of the FGC is assumed to be 350um, thus allowing a $150\mu m$ mounting distance of the sample from the integrated OCT chip. These two values give a rough first hand estimate of the FGC numerical aperture, which in turn can be interpreted to the size of the FGC. This led to a size of $40\mu m$ by $40\mu m$ FGC.

3.2 Modeling and simulation methods

To design an FGC optimized with respect to these parameters, an efficient analysis tool and accurate characterization methods are required. An accurate analysis of curved and chirped grating structure requires a fully vectorial three-dimensional calculation. But this is computationally challenging as due to the structures complexity and the large area of the FGC. Thus a simple and approximate treatment is the usual option to analyze the characteristics of FGCs.

To calculate the outcoupling efficiency of the FGC, we considered the grating structure in the central line of the FGC as it is this part of the FGC that mainly dominates its characteristics. Thus, it will turn out to be a 2D calculation, which is relatively easier to analyze. For this problem, a simulation tool developed at Ghent University Photonics Research Group called CAvity Modeling Framework (CAMFR)[32] is used. This simulation tool is based on the principle of eigen mode expansion.

For calculating the focusing performance of the FGC, we opted to use a perturbation expansion method adapted for FGC [33]. As the formulation given in this paper doesn't consider the exponential decay of the guided wave as it scatters from the corrugations, a correction factor is added by calculating the decay constant for the grating structure in the central line of the FGC. The intensity decay factor is calculated using CAMFR.

3.2.1 Eigen mode expansion method and CAMFR

The eigen mode expansion method is a well established Maxwell equation solving approach in photonics. The main essence is to divide a structure into waveguides where the refractive index doesn't vary in the z direction. This enables to easily write the solution of the mode in each section. And hence, the solution of the structure can be written as a series sum of modes. Each mode is characterized by its mode profile and mode index. Appropriate boundary conditions can be applied at each boundary of the sections to allow continuity of fields. In a typical waveguide, guided modes and radiation modes together will form a complete basis set, thereby enabling to express any solution of Maxwell's equations in the region of the waveguide in terms of a superposition of the forward and backward propagating modes.[34]

CAMFR is a Maxwell solver which uses eigen mode expansion technique. It enables to calculate the scattering matrix of a structure, field inside a structure as per specified excitations, and other related calculations. It is best suited to analyze 2D gratings. In a uniform grating, each slab waveguide can be concatenated together to form a stack. The stack defines the entire structure. All the quantities that can be known about the stack (such as Reflection, Transmission, field values at any point in the computational space, etc) can be calculated.[32]

In our analysis, the structure along the FGC central axis is considered. We assumed it to have index invariance in the y-direction. So, it becomes a 1D chirped grating. Each period is calculated from the main grating line equation, (3.3). So, the grating structure can be formed by appending slab waveguides having widths of the calculated periods into a stack. Guided mode of the waveguide is used as an excitation. And appropriate parameters, such as the decay constant, outcoupling efficiency, reflection, and transmission are calculated.

3.2.2 The perturbation expansion method

We used the perturbation expansion method to simulate the focusing performance of the FGC. The development presented here follows the formulation given in Joel.[33] In a perturbation analysis the grating is treated as a small perturbation of the waveguide structure without the grating. This method considers a three layer structure (substrate, film and cover). The SOI corresponding counter parts are the $1\mu m$ thick SiO2 layer for substrate, the $220nm$ thick Si layer for film, and air for cover. The field at the surface of the grating is perturbed due to the surface roughness. This helps to write the field at air-waveguide interface as a power series expansion. This method will be applied to the specific problem to obtain the diffracted field at the exit pupil of the focusing grating couplers. Kirchhoff's diffraction formulas are subsequently employed to compute the field at the focal plane of the grating coupler.[35]

3.2.3 Geometry of Problem

Before we begin, we should first define the geometry of the problem that we are investigating. The general focusing grating coupler for this problem is shown below in figure 3.2. The grating coupler lies in the y-z plane with the origin *0* in the center of the grating. The guided wave propagates in the y-z plane and is coupled by the focusing grating coupler out of the waveguide and focused into the focal spot *F*. The focal spot is located in the x-z plane, a distance f from the origin. Figure 3.3 shows the grating layer.

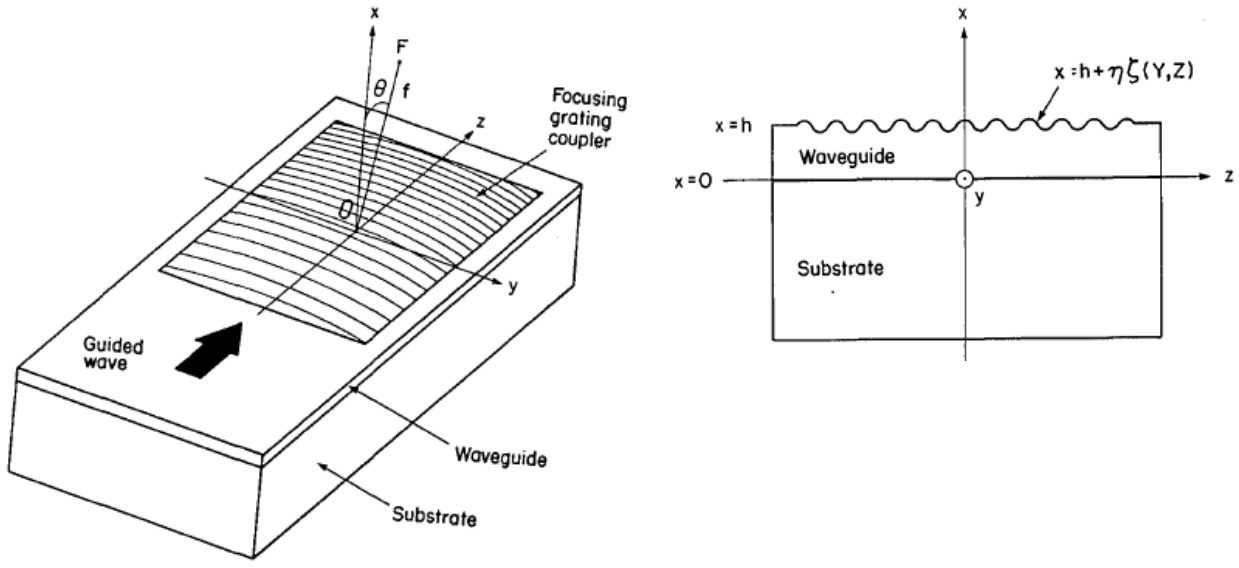

(a) (b)

Figure 3.2: (a)Focusing grating coupler on SOI platform (b) layer structure of the FGC

The structure consists of four regions: region I- the cover, in this case it is air with refractive index $n_c = 1$, region II is the film (or the waveguide) which is the Si layer in the SOI platform and has refractive index of $n_f = 3.46$, region III is the SiO2 substrate and has index of $n_s = 1.47$, and region IV is the $7\mu m$ thick Si substrate, but this part of the layer is not considered in the simulation, due to the complicated mathematics.

3.2.4 Adaptation of the perturbation method for FGC calculation

Figure 3.2(b) shows a schematic configuration of the FGC layer structure. The waveguide-substrate boundary is located at the $x = 0$ plane, and the waveguide-cover interface is given by

$$x = h + \eta\zeta(y, z) \qquad (3.4)$$

Here h is the average thickness of the waveguide, η is related to the amplitude of the corrugation, and $\zeta(y, z)$ defines the profile of the corrugation and is determined by the wavefront phase difference between the input wave and the outcoupled wave phase front.
Let the input guided wave has a mode profile of

$$\vec{E}_{in} = E_o \exp(i\beta z) \qquad (3.5)$$

To obtain the functional form of $\zeta(y, z)$, we consider the grating to have been fabricated holographycally through the interference of a spherical wave emanating from the focal point F and a guided wave propagating in the negative *z*- direction. This gives:

$$\zeta(y, z) = \exp\{-i[\beta z + k_o R(y, z)]\} + complex\ conjugate \qquad (3.6)$$

where $\exp(-i\beta z)$ corresponds to the mode of the input guided wave, and $\exp[-ik_o R(y, z)]$ refers to a spherical wave emanating from the focal point F, to a point $(0, y, z)$ on the surface of

the grating. The amplitudes are omitted as only the phase relationships determine the grating pattern.

The electric field and magnetic fields can be expressed in terms of the vector potential. The corrugation can be considered as a perturbation of the surface of the grating, which transforms to the perturbation of the waveguide mode. Thus, the vector potential can be expanded as a power series of η and will take the following form for the three regions of the grating layer:

$$\vec{A}_I = \vec{A}_i^I + \sum_{n=1}^{\infty} \eta^n \vec{A}_{sn}^I \qquad x > h,$$

$$\vec{A}_{II} = \vec{A}_i^{II} + \sum_{n=1}^{\infty} \eta^n \vec{A}_{sn}^{II} \qquad 0 < x < h,$$

$$\vec{A}_{III} = \vec{A}_i^{III} + \sum_{n=1}^{\infty} \eta^n \vec{A}_{sn}^{III} \qquad x < 0,$$

The $\vec{A}_i$'s refer to the unperturbed field, and the $\vec{A}_{sn}$'s correspond to the nth-order scattered field. The $\vec{A}_I$, $\vec{A}_{II}$, $\vec{A}_{III}$ should satisfy the Maxwell's wave equations in the respective regions. Moreover, they should satisfy the transversality condition and the respective boundary conditions in each region.

The analysis assumes a TE polarized wave input mode:

$$\vec{A}_i = Aexp(i\beta z)\hat{e}_y \qquad (3.8)$$

where *A* is the input mode amplitude and is independent of the y-coordinate.

But, this incident wave is perturbed at the interface between the waveguide and the cover layers*(x=h),* and can be expressed as a series in powers of η:

$$\vec{A}_i^I = \vec{A}_i^I\big|_{x=h} + \left.\frac{\partial \vec{A}_i^I}{\partial x}\right|_{x=h} \eta\xi + \left.\frac{\partial^2 \vec{A}_i^I}{\partial x^2}\right|_{x=h} \eta^2\xi^2 + \cdots \qquad (3.9)$$

Putting these expressions into the boundary condition requirements and doing some mathematical trick, one arrives at the following simplified expression for the field values on the surface of the grating:

$$\vec{A}_I(0,y,z) = \eta\vec{U}(q_y,q_z)\exp[-ik_oR(y,z)] \qquad (3.10)$$

where the value of $\vec{U}(q_y,q_z)$ is given in the paper of Joel[33].

The analysis given in Joel[33], doesn't take into account the exponential decay of the guided field as it propagates inside the grating due to outcoupling. Inclusion of this effect is done by calculating the decay factor of the mode using the CAMFR simulatison tool.
Including the exponential decay term in (3.10), the expression for the field profile takes the form:

$$\vec{A}_I(0,y,z) = \eta\vec{U}(q_y,q_z)\exp\left[-\alpha(\frac{L}{2}+z)\right]\exp[-ik_oR(y,z)] \qquad (3.11)$$

where $\vec{U}(q_y,q_z)$ are the same expressions given in [33].

Thus, this modified expression can be used to calculate the field values at the surface of the grating, and the appropriate Kirchoff's diffraction formulas can be used to calculate the field at the focal plane.

This model assumes the wavelength of the input guided light to be the same as the design wavelength of the FGC. Additional derivations are needed to formulate a general expression that is valid for any wavelength of the input guided wave. The derivation is given in appendix I.
The results are:

$$\vec{A}_I(0,y,z) = \eta\frac{\vec{U}(q_y,q_z)\exp[-\alpha(\frac{L}{2}+z)]}{\sqrt{1-2(\beta-\beta_o)\frac{z}{k_oR}-\frac{(\beta-\beta_o)^2}{k_o^2}}}exp\left\{-i[k_oR(y,z)-\frac{(\beta-\beta_o)}{2}z + \frac{(\beta-\beta_o)^2}{4k_o}R]\right\} \qquad (3.12)$$

Where

$$\beta_o = \frac{2\pi}{\lambda_o}n_{eff} \qquad and \qquad \beta = \frac{2\pi}{\lambda}n_{eff}$$

λ_o refers to the wavelength of the guided input wave where the FGC is intended to couple out, and λ is that of the input guided wave.

The exponential decay is also taken into account. This expression reduces to the original equation of [33] when input guided wave wavelength matches the design wavelength of the FGC.

3.3 Numerical results

The models and techniques discussed in section (3.2) are applied to calculate the intensity decay constant, reflection, efficiency, beam width at the focus plane, and chromatic dispersion properties of the FGC. The calculations are made for an FGC of size $40\mu m \times 40\mu m$. The focal length is assumed to be $350\mu m$. The table below shows the average period for the FGC design with different focusing angles. For all the calculations a filling factor of 0.5 is assumed. The effect of filling factor on uniform grating performance is discussed in [27]. It is shown that a filling factor of 0.5 does give better efficiency and lower back reflection.

θ	0^o	8^o	15^o
Average period(μm)	0.543	0.575	0.602
Number of periods	72	69	65

Table 3.1: The average period of the grating structure along the central line of the FGC for different focusing angles.

3.3.1 Calculation of decay constant, reflection, and efficiency

In this section we present the results for the calculation of the decay constant, reflection and efficiency of the grating structure along the central line of the FGC. The SOI structure used in the simulation is shown in Figure 3.3 below. The structure is uniform in the y-direction. For the calculation, a TE mode input guided wave is assumed. The CAMFR simulation is done for different etch depths. The python script used for the simulation is given in appendix (III).

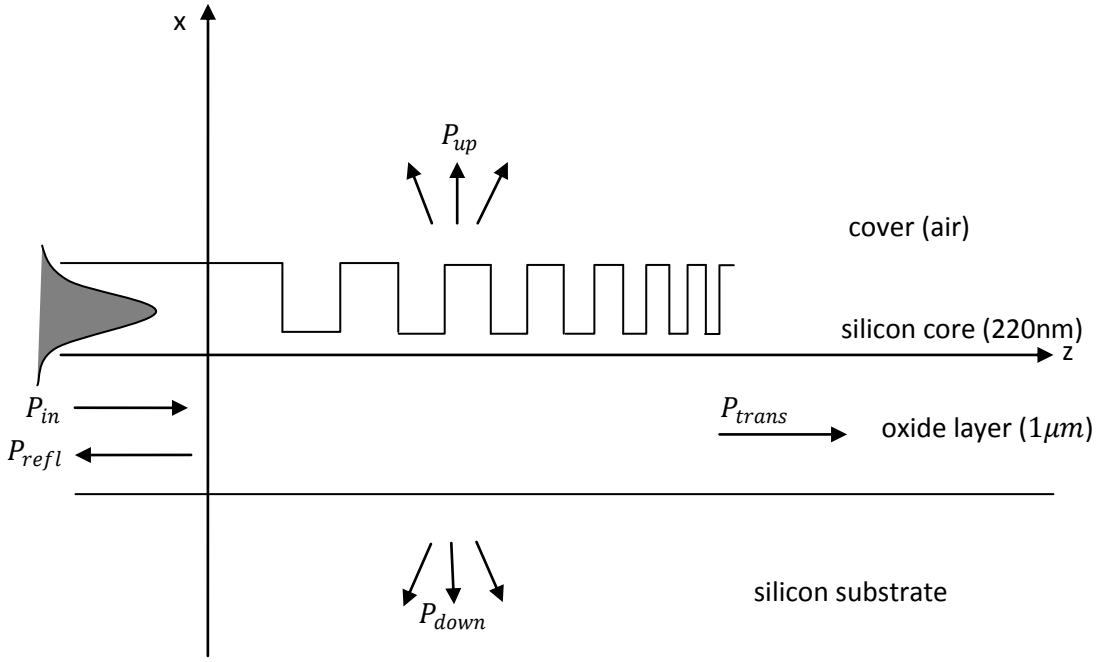

Figure 3.3: The grating structure along the central line of the FGC

Figure 3.4 shows the decay constant variation with groove depth for three different outcoupling angles. The decay constant tends to be a bit higher for higher focusing angle. This is due to the relatively longer grating period. It is also higher for deeper grooves. The decay constant dictates the selection of the grating length. Longer FGCs require smaller groove depth, and hence lower decay constant; otherwise the input guided wave will be lost before traversing appreciable distance inside the grating.

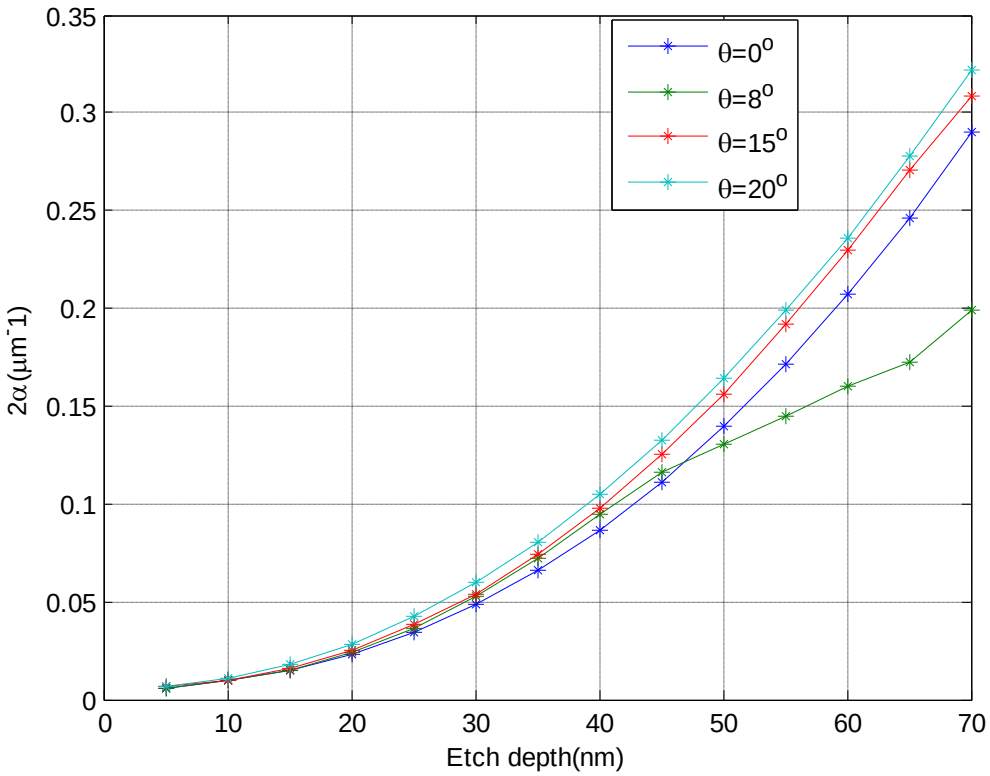

Figure 3.4: Intensity decay constant versus groove depth for different outcoupling angles.

Figures (3.5),(3.6) &(3.7) show the reflection R as a function of wavelength for different etch depths for outcoupling angles of $0^o, 8^o, 15^o$ respectively. Generally, the reflection increases as the etch depth increases. Also the peak reflection shifts to the lower wavelength region because the effective refractive index is smaller for deeper grooves.

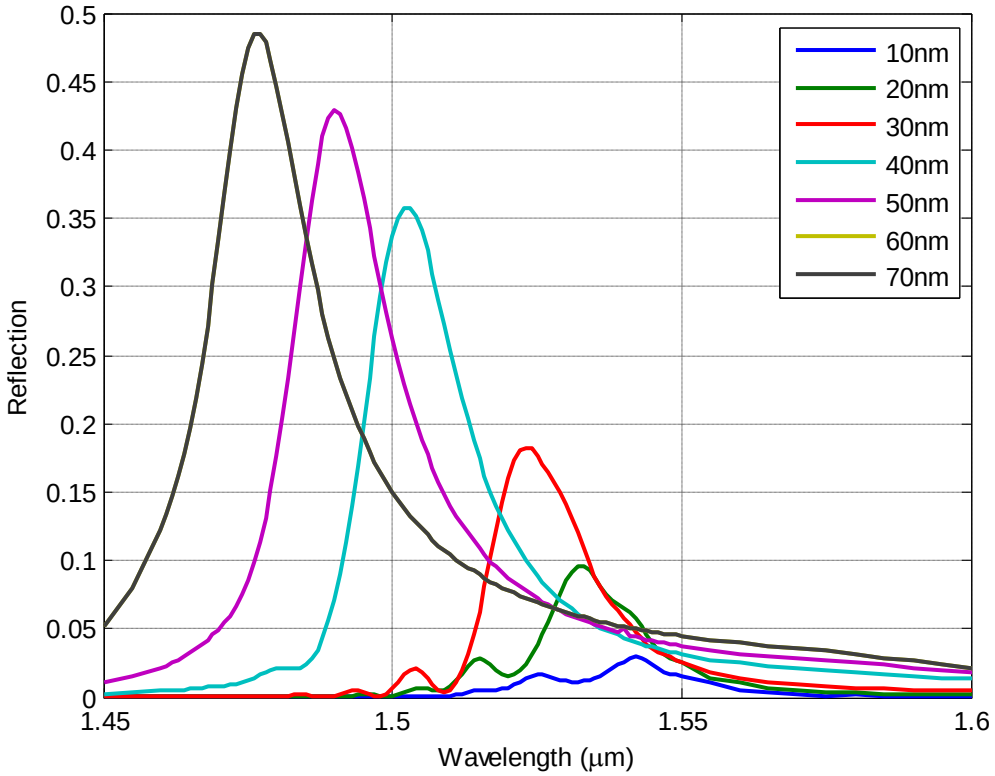

Figure 3.5: Reflection versus wavelength for $\theta = 0^o$

For vertical outcoupling ($\theta = 0$), the reflection is less than 5% at the center wavelength(*1550nm*) for all etch depths. But, it gets higher for wavelengths below the central wavelength except for the 10nm groove depth. But, the 10nm grove depth gives small outcoupling efficiency. This seriously limits the use of FGC for vertical outcoupling in broadband applications.

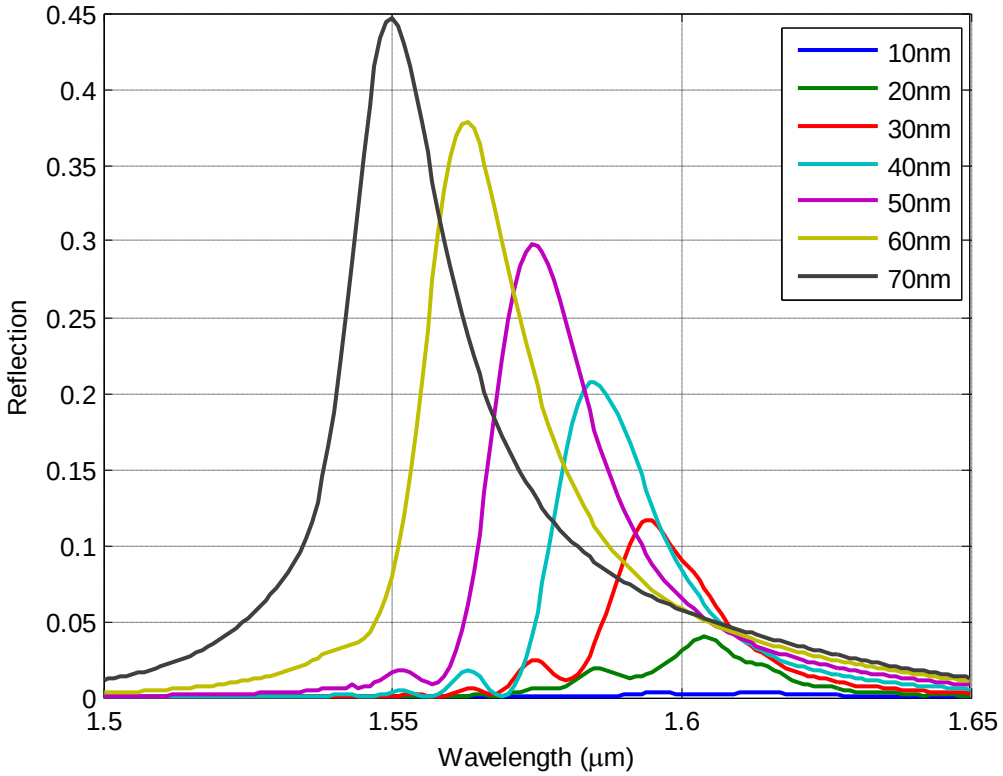

Figure 3.6: Reflection versus wavelength for $\theta = 8^o$

The reflection for focusing angle 8^o is not ideal either. The reflection around the center wavelength is higher for all etch depths except the 10nm, 20nm, and 30nm. The relative higher efficiency of 30nm groove depth makes it appropriate for this design.

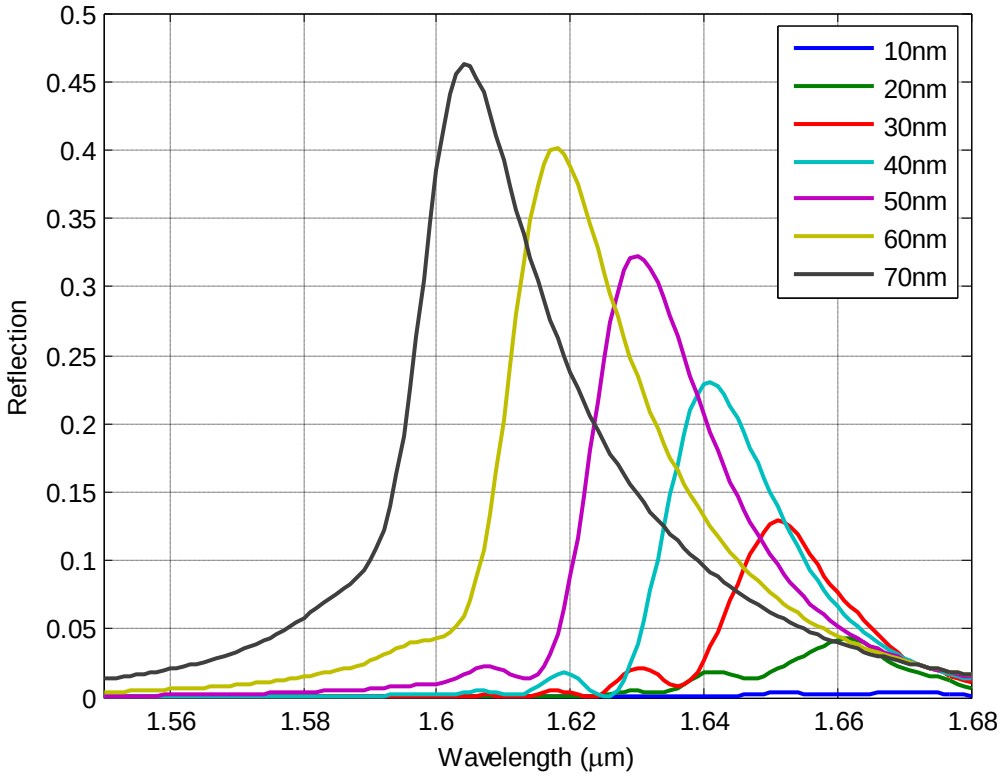

Figure 3.7: Reflection versus wavelength for $\theta = 15^o$

Figure (3.7) shows the reflection versus wavelength for different groove depths for coupling angle of 15. The reflection at the center wavelength is below 5% for all groove depths. Around the center wavelength, the reflection is low enough even for grooves as deep as 70nm.

Figure 3.8(a&b) shows the coupling efficiency for an FGC with 0^o outcoupling angle, having groove depths 30nm and 70nm respectively. Comparison is made with the reflection plot as well. As expected the efficiency is lower around wavelengths where the reflection peaks.

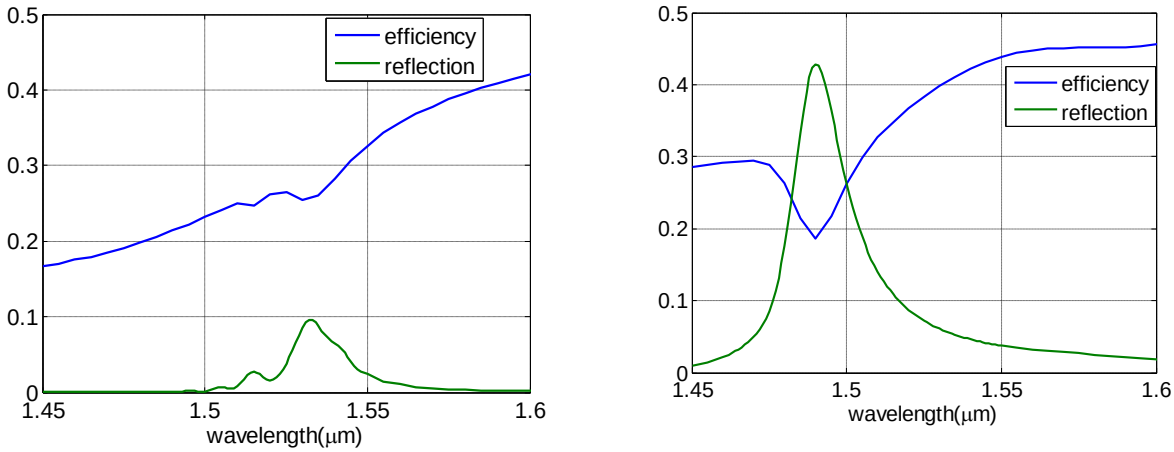

(a) (b)

Figure 3.8: Efficiency and reflection for $\theta = 0^o$ with groove depths (a) *30nm* (b) *70nm*

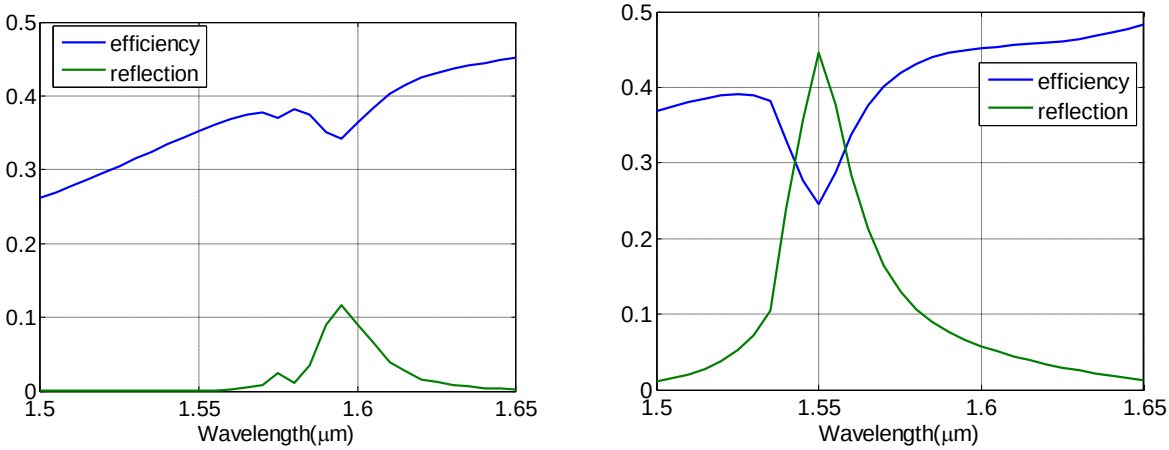

(a) (b)

Figure 3.9: Efficiency and reflection for $\theta = 8^o$ with groove depths (a) *30nm* (b) *70nm*

Figure (3.10a) &(3.10b) shows the coupling efficiency for an FGC with 8^o outcoupling angle , having groove depths 30nm and 70nm respectively. The outcoupling efficiency is better for focusing angle of 8 than vertical outcoupling. This can be attributed to the fact that the back reflection in case of vertical coupling is relatively higher. Again, the efficieny tends to be higher for deeper grooves. As expected, the outcoupling efficiency is lower at wavelengths where the

back reflection peaks. Unless we work on applications which require backreflection, it is better to operate at wavelengths away from reflection peak points to get good efficiency.

Figure 3.11 shows the field plot for the FGC structure along its central axis. It is calculated for an FGC with outcoupling angle of 8^o. Groove depth of 30nm is assumed.

Figure 3.10 shows the field plot obtained for the grating structure along the central line of the FGC. The calculation is done for $\theta = 8$, and etch depth of 30nm.

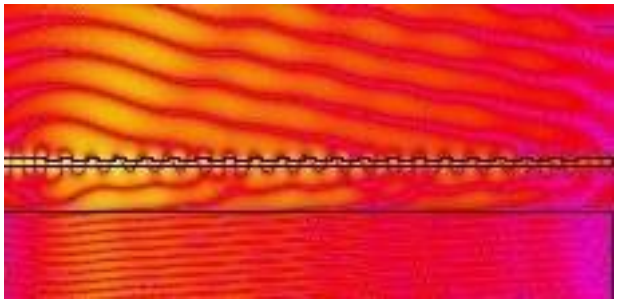

Figure 3.10: Field plot for the FGC structure along its central line. $\theta = 8$, groove depth = 30nm.

3.3.2 Calculation of beam spot size at the focal plane of the FGC

The focusing performance of an FGC is determined by the 3dB spot width of the outcoupled wave intensity. The above formulations have been used to calculate the field profile on the surface of the grating. Then the Kirchhoff's diffraction theory has been applied to calculate the corresponding field profiles on the focal plane of the focusing lens. To this end a Matlab routine (see appendix IV) was written. The results are summarized below.

Figure (3.11) shows the intensity profile on the focal plane. The simulation is done for an etch depth of 30nm. The results show that the field profiles along y and z are symmetrical. The FWHM of the intensity profile is $12.6\mu m$.

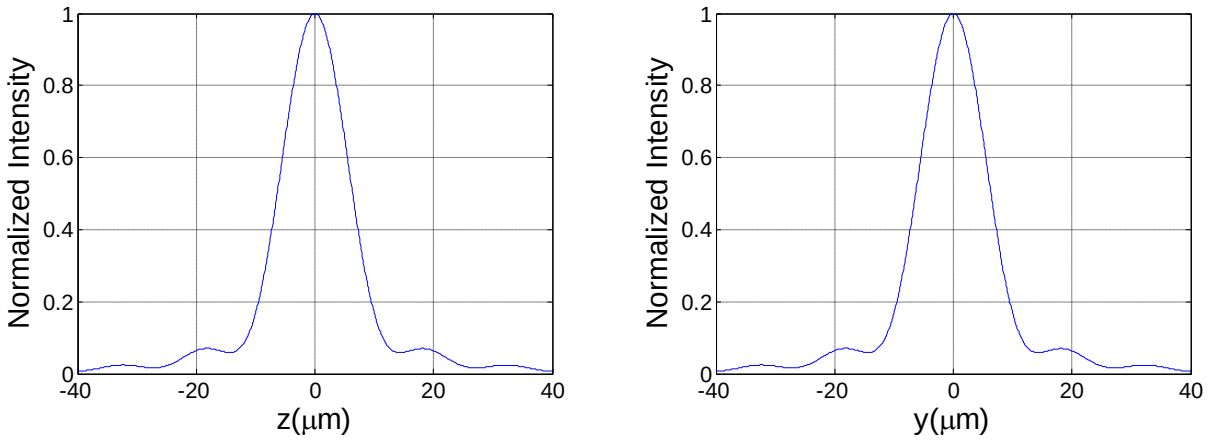

(a) (b)

Figure 3.11: Intensity Profile on the focal plane along (a) z axis and (b) along y axis

The intensity profile is also calculated for different grove depths. The result is shown in Figure (3.12). The corresponding spot size variation with groove depth is also shown in figure 3.13. As can be seen from the graph, the spot size increases when the grove depth of the FGC increases. This can be attributed to the fact that the intensity decay factor is very higher for deeper grooves. Highly etched grating tits cause much scattering, hence introducing high decay constant. This causes distortion of the outcoupled beam profile.

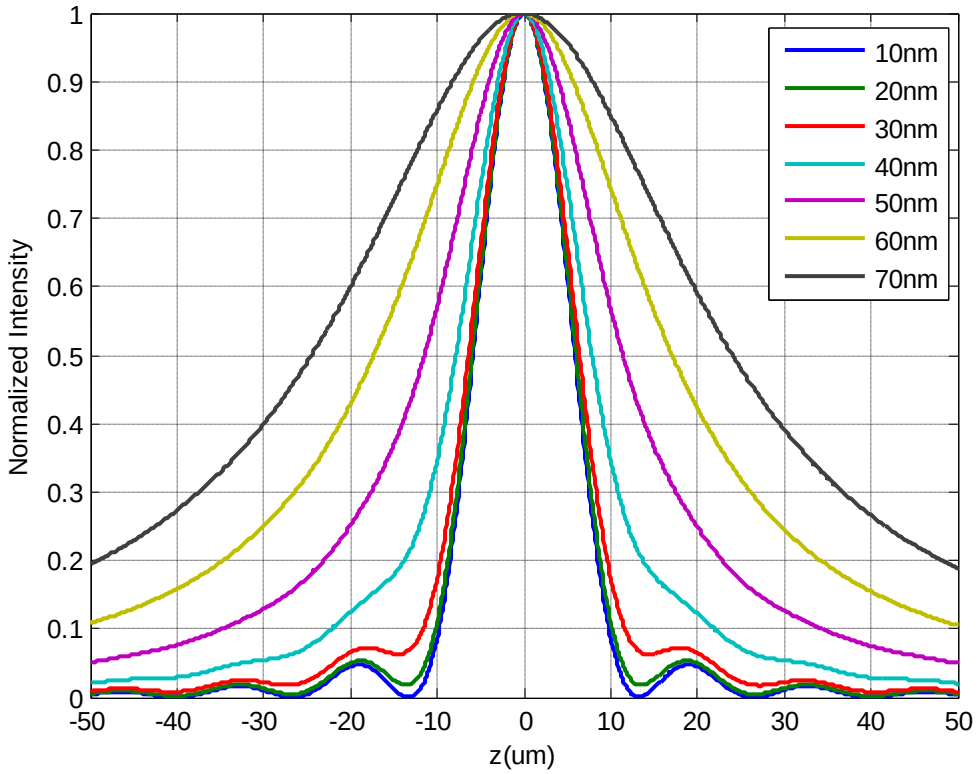

Figure 3.12: Intensity profile on the focal plane of the FGC for different etch depths.

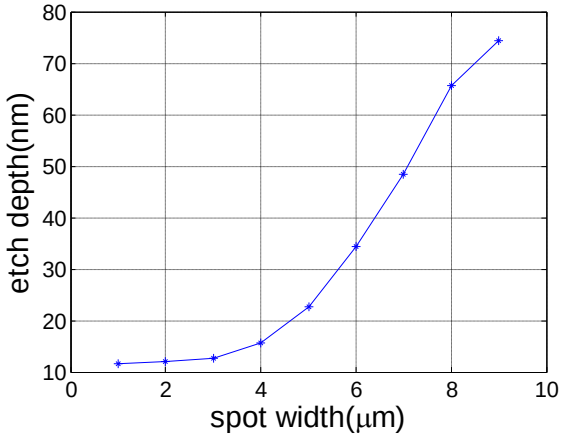

Figure 3.13: Outcoupled beam width at the focal plane for different groove depths.

3.4 Chromatic aberration of the FGC

The grating equation which determines the pattern of the grating lines is a function of wavelength. When the input guided wave wavelength differs from the design wavelength of the FGC, a shift in the focus point of the outcoupled wave is observed. The expression derived in sec. (3.2.3) is used to calculate the field profile of the FGC for input wavelengths different from this central wavelength. The result is given in Figure 3.14. It shows how the focus point moves when the wavelength of the input guided wave changes.

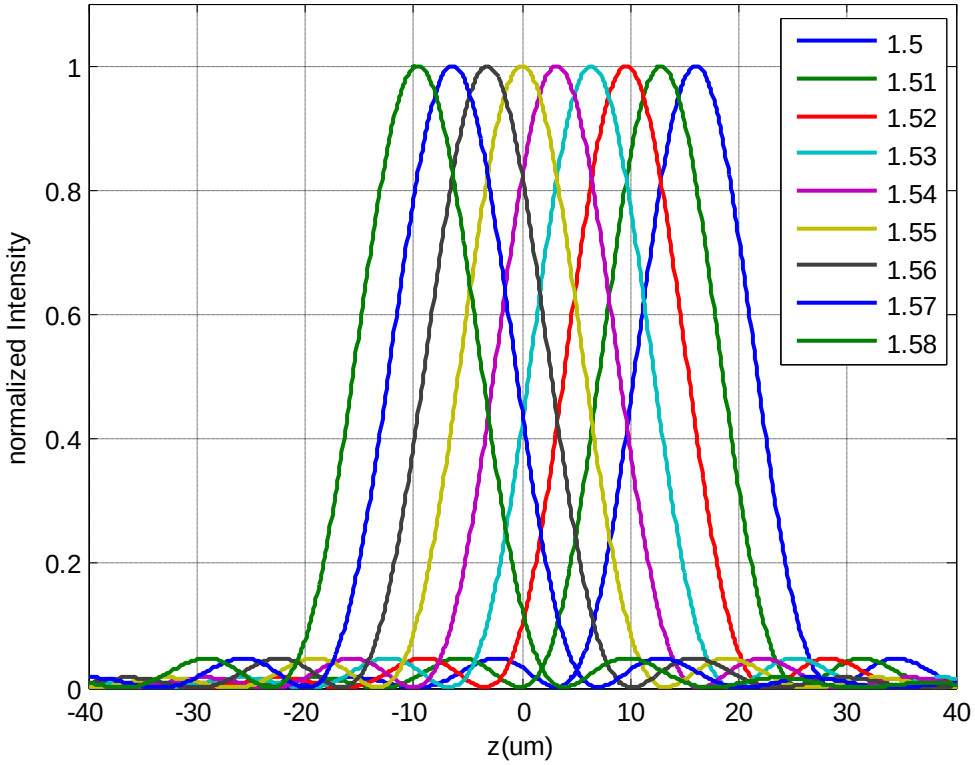

Figure 3.14: The normalzed intensity profile at the focal plane for input waves of different wavelengths. The FGC is designed for input wavelength of $1.55\mu m$.

This chromatic aberration decreases the overall bandwidth of the FGC. It deteriorates the transverse resolution of the FD-OCT. The source of FD-OCT is broadband and hence the bandwidth of the FGC is an important parameter to calculate.

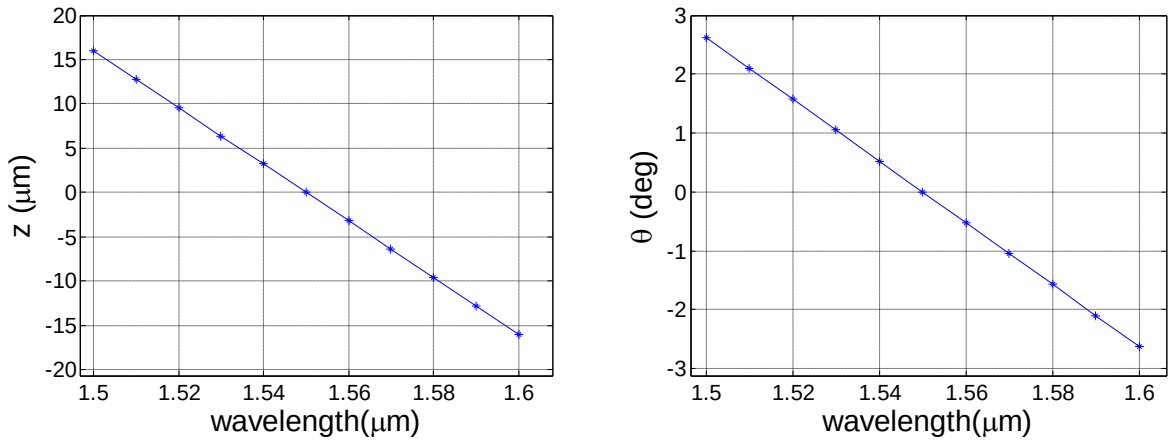

(a) (b)

Figure 3.15: Dispersion of the FGC (a) position of the focus point along z-direction (b) angle shift of the focus point from the x-direction for different

Figure (3.15) shows the dispersion of the Focusing grating coupler. The averaged dispersion is around $0.368\mu m/nm$. Our OCT system is meant to have a transverse resolution of approximately $20\mu m$. The dispersion of the FGC should be within this resolution range. Thus, from dispersion point of view and the resolution requirement of the FGC, the bandwidth of the focusing grating coupler becomes $\frac{20}{0.368} \approx 54nm$.

3.5 Conclusion

Highly etched gratings do give high outcoupling efficiency, but the higher intensity decay constant makes them unsuitable for longer FGCs. High intensity decay constant causes distortion of the outcoupled light beam, and hence results in large focus spot size. In wavelength region where the back reflection peaks, the outcoupling efficiency drops. This can be overcome by shifting the operation region to other wavelength, or by tuning the outcoupling angle to so that the back reflection doesn't peak at the particular operational wavelength range.

Chapter 4

Fabrication and Measurement

In this chapter we provide an overview of the technology used to fabricate the integrated photonics circuit of the OCT system and discuss the measured results. First, we introduce the method used to design the mask, and the processing scheme used to fabricate the integrated photonic circuit. Then, we discuss the measurement setup used for the characterization of the chip, and finally the obtained measurement results are presented.

4.1 Mask design

The first step before fabrication is the design of the mask layout. Mask is a blue print that carries the pattern of the device to be fabricated. The lithography process transfers the pattern on the mask to the SOI wafer.

For the mask layout design, we used Python based libraries developed in our group. There are two basic libraries: IPKISS and PICASSO[36]. The IPKISS library contains many basic geometrical shapes with corresponding methods to manipulate the shapes. Using these shapes it is possible to create a mask layout for the nanophotonic component. PICASSO is a much more comfortable library since it contains not merely basic shapes, rather basic photonic components. Using these design tools, we wrote scripts to generate the mask file for each components of the OCT system according to the optimized parameters from the simulation results. Each component is connected to build up the whole system. The scripts used to generate the mask GDSII file is given in appendix IV. Figure 4.1 shows the mask of the OCT system. The circuit has a footprint of 6x2 mm, out of which the PCG takes a 5x2 mm area. Individual components are given in Figure 4.2 with a higher magnification.

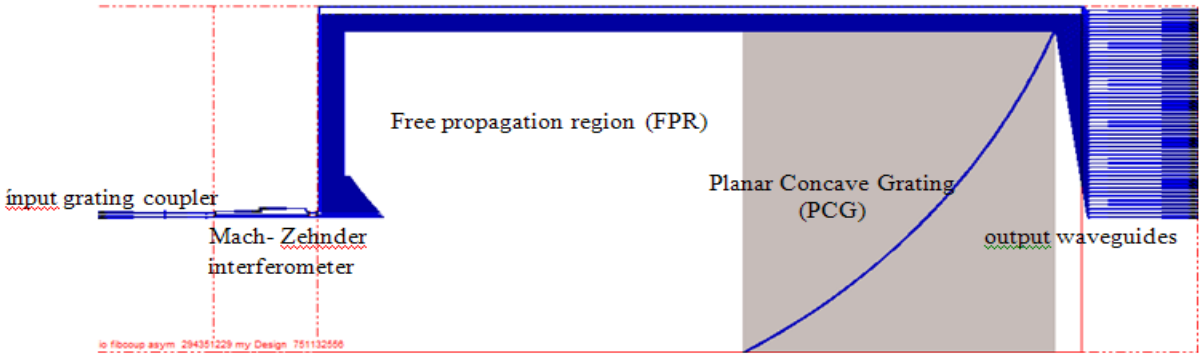

Figure 4.1: The mask layout of the OCT system

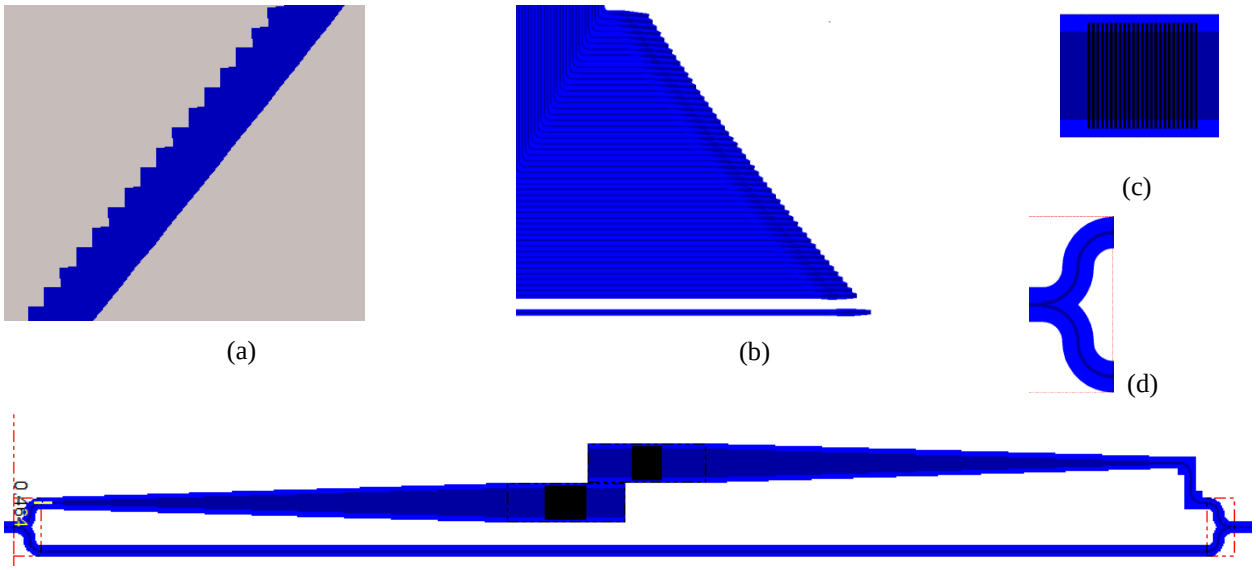

Figure 4.2: Components of the OCT system photonic IC (a) PCG facets, (b) output and input waveguides of the PCG, (c) the grating coupler (d) the splitter,(e) the Mach-Zehnder interferometer. Not all pictures are at the same scale.

4.2 Fabrication

The high index contrast of the Silicon-on-insulator (SOI) material system enables the realization of wavelength scale photonic structures. The drive for the adoption of SOI platform for photonics integration is its compatibility with the well developed CMOS fabrication

technology for electronic integrated circuits. The integrated OCT system we designed was fabricated using the CMOS fabrication based processing scheme[37] [38]. The fabrication is done using the state-of-the-art CMOS processing tools of IMEC, Belgium.

The fabrication involves deep UV lithography and dry etching. The general processing scheme of this technology is shown in figure 4.3

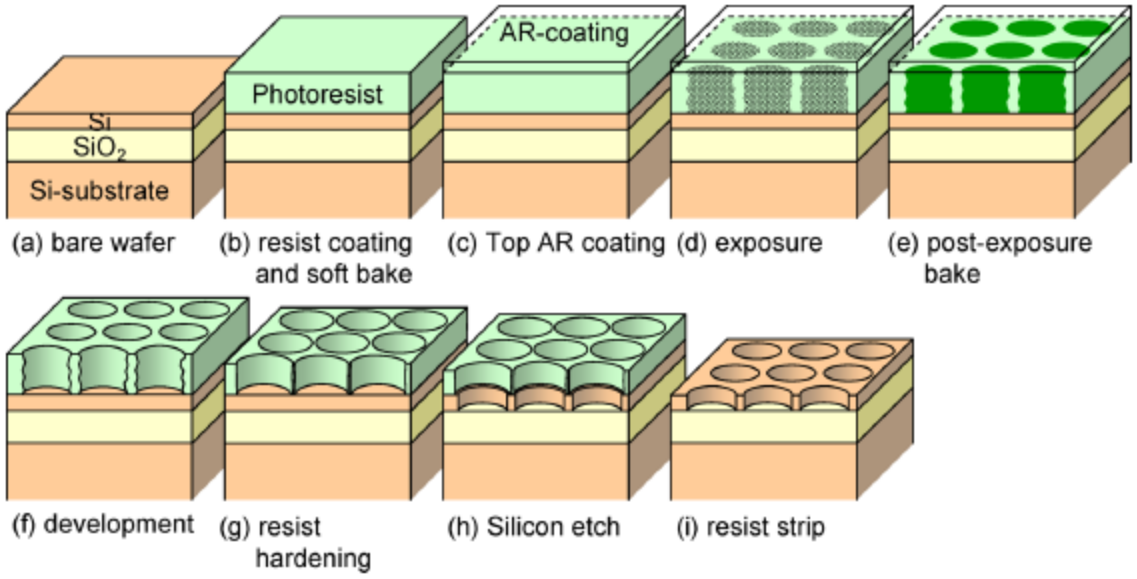

Figure 4.3: Fabrication process for nanophotonic structures in SOI using deep UV lithography and dry etching.

First the SOI wafer is coated with a photoresist, and it is prebaked. Then anti reflection coating is deposited on top of it. Afterwards, it is illuminated by using a deep UV stepper. Following the illumination, it is baked and developed.

After the lithography, the pattern of the photoresist is transferred to the SOI using dry etching.The top Silicon layer is etched with a low pressure Inductively Coupled Plasma (ICP) etching based on *Cl*2/*HBr*/*He*/*O*2. This is a highly selective etch process. Subsequently, the oxide was etched using medium density *CF*4/*O*2-plasma chemistry at medium pressure.

For the definition of the PCG facets, the Silicon top layer is completely etched. A more shallow etch (*70 nm*) was used for the definition of the 2.25-μm-wide entrance and exit waveguides of the PCG [39]. The deeply and shallowly etched structures are defined in separate lithography and etch steps. The transition between deep and shallow waveguides is done using a

short but adiabatic transition structure[39]. The grating couplers are defined using a shallow etch step[40] [41].

Figure 4.4 shows a scanning electron microscope (SEM) images grating facets and output waveguides of the PCG and a general light microscope image of all output waveguides.

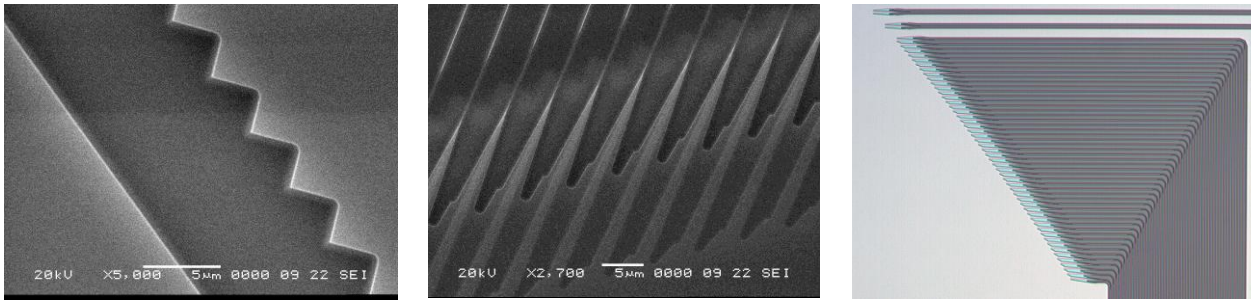

(a) (b) (c)

Figure 4.4: (a) SEM image of grating teeth (b) SEM image of grating output waveguides (c) Microscope image of input and all output waveguides of the PCG

4.3 Measurement

For characterization of the fabricated chip, we used the measurement facility of our research group. The measurement setup used is shown in Figure 4.5.

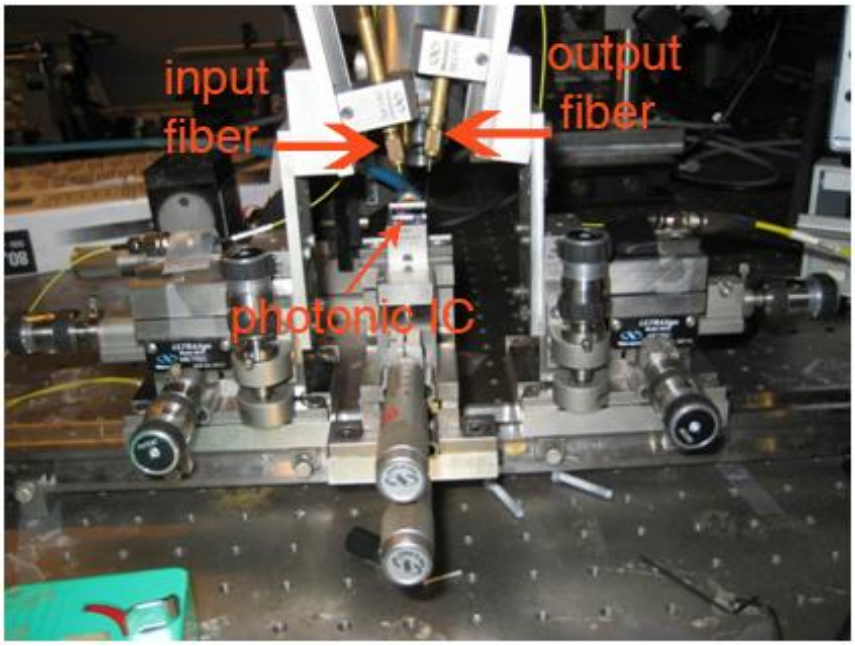

Figure 4.5: Measurement setup used for the characterization of the photonic integrated circuits.

Light is coupled in and out of the photonic circuit using grating couplers at both ends of the sample to a fiber. The chip is mounted on a 2D translational stage. The input and output fibers are mounted on a 3-D translational stages. Since the grating couplers efficiency is optimized for 10^{o} fiber alignment, the fibers are mounted with this angle from the vertical direction. The input fiber is connected to our source, a super-luminescent diode (SLD). The output fiber is connected to an optical spectrum analyzer. The optical spectrum analyzer is connected to a computer through a GPIP interface.

There is a CCD camera connected to a monitor to facilitate the input/output fibers alignment. When the lamp illuminates the chip and the fibers, it allows clear observation of the chip and the fiber. When the fiber is close to the chip surface, it casts a shadow on the sample. Following the relative position of the fiber and its shadow, it is possible to make an initial alignment of the fiber. Once, we manage to get some output power, further alignment can be done by slowly moving the fiber in three directions until we get the maximum output power possible. The input and output fibers we used are standard single mode fibers. There is also a polarization controller just before the input fiber. It can be used to further maximize the transmission since all the photonic components of the chip are optimized for TE light.

4.3.1 Characterization of components of the Mach-Zehnder interferometer

The first measurement is done to check the coupling efficiency of the input/output grating couplers. To this end, a simple waveguide is used as a sample. We measured the transmission spectra from the input grating coupler to the output grating coupler via the waveguide. A transmission loss of 18dB was measured. Since the waveguide is short, the loss due to the waveguide can be neglected, which implies that the coupling loss is 9 dB per grating coupler. The measured spectrum is shown in figure 4.4(a).

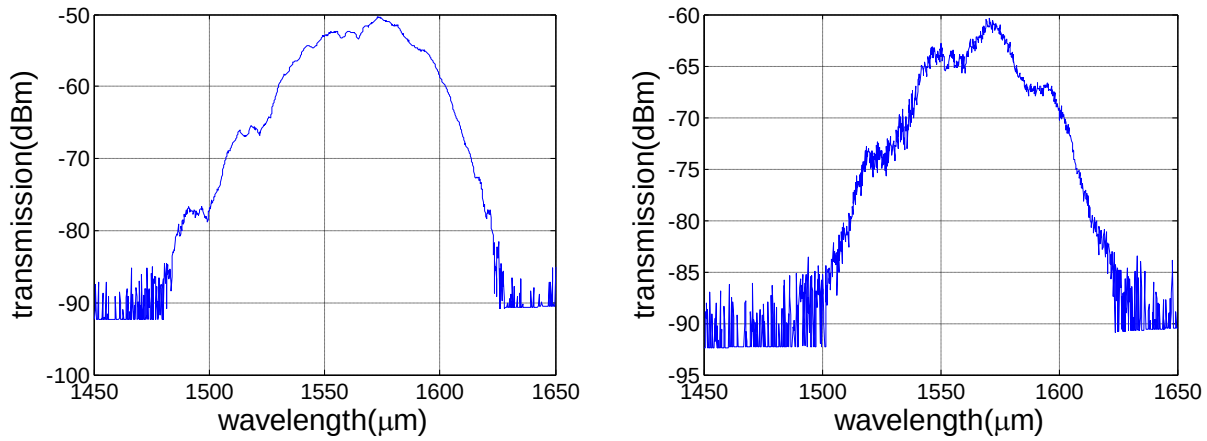

Figure 4.3: transmission spectra of (a) sample waveguide (b) reference waveguide of the Mach – Zehnder interferometer

We also measured the transmission for a reference structure. The reference structure is shown in Figure 4.4. It consists of the lower arm of the Mach-Zehnder and an additional splitter which splits the output of the MZ into two: one to the input waveguide of the PCG, the other connected to a grating coupler which enables this characterization. The reading from the reference output can be used to normalize the transmission of the PCG.

Figure 4.4: The reference structure used to normalize the PCG reading

The measured spectrum is shown in figure 4.3(b). It has a loss of 31dB. Accounting 18dB for the input/output gratings and 1dB for waveguide loss, the loss per splitter becomes 4dB, rather than ideal 3dB. The spectrum of the reference structure is perturbed as compared to the spectrum of the simple waveguide. This can be due to multiple reflections within the system, notably from the grating coupler on the upper arm of the Mach-Zehnder interferometer.

4.3.2 Characterization of the Spectrometer

The above measurement setup was used to measure the spectral response of the PCG spectrometer. A broadband light from the SLD is coupled to the input waveguide and we measured the power from each of the 50 output channels. The measured result is normalized with respect to the reference structure measurement above. The obtained result is shown in figure 4.5. It gives the response for the 42 channels. The power outputs for the remaining eight channels were below the instrument noise level.

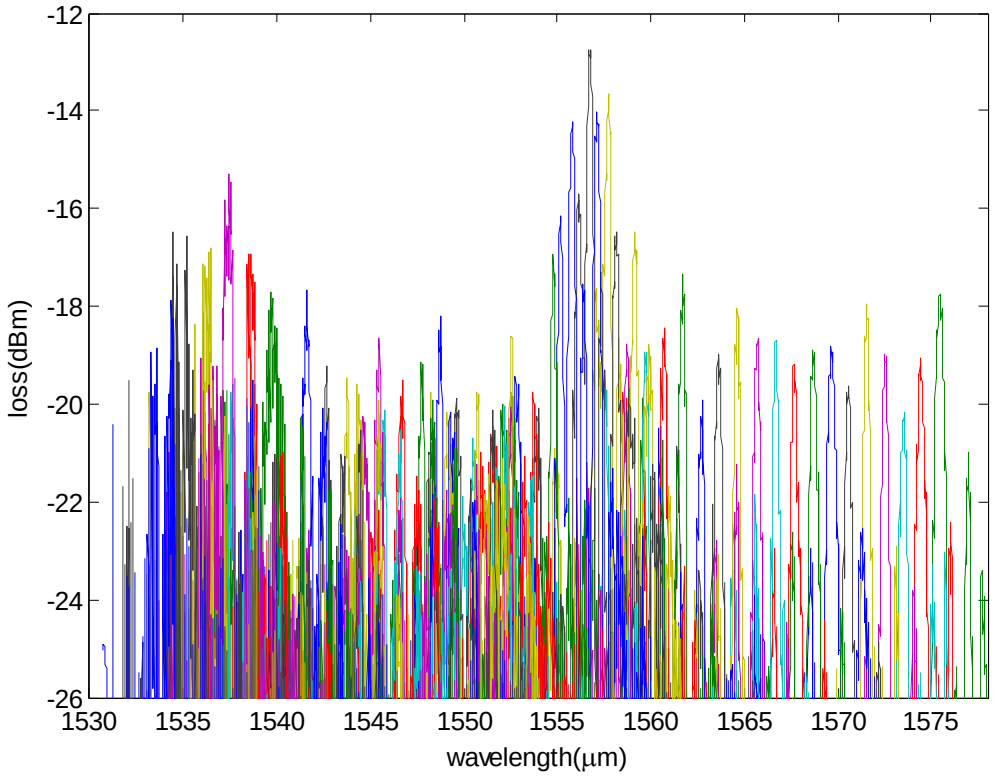

Figure 4.5: Spectral response of the PCG

As anticipated from the simulation studies, the loss is minimum for the central channel, but gets worse towards the peripheral channels. The fiber-to-fiber insertion loss is 13.0dB for the central channel. The average loss variation is around 0.25dBm per channel.

Figure 4.6 shows a more detailed spectrum .Generally, the spectral response is relatively better for the longer wavelengths.

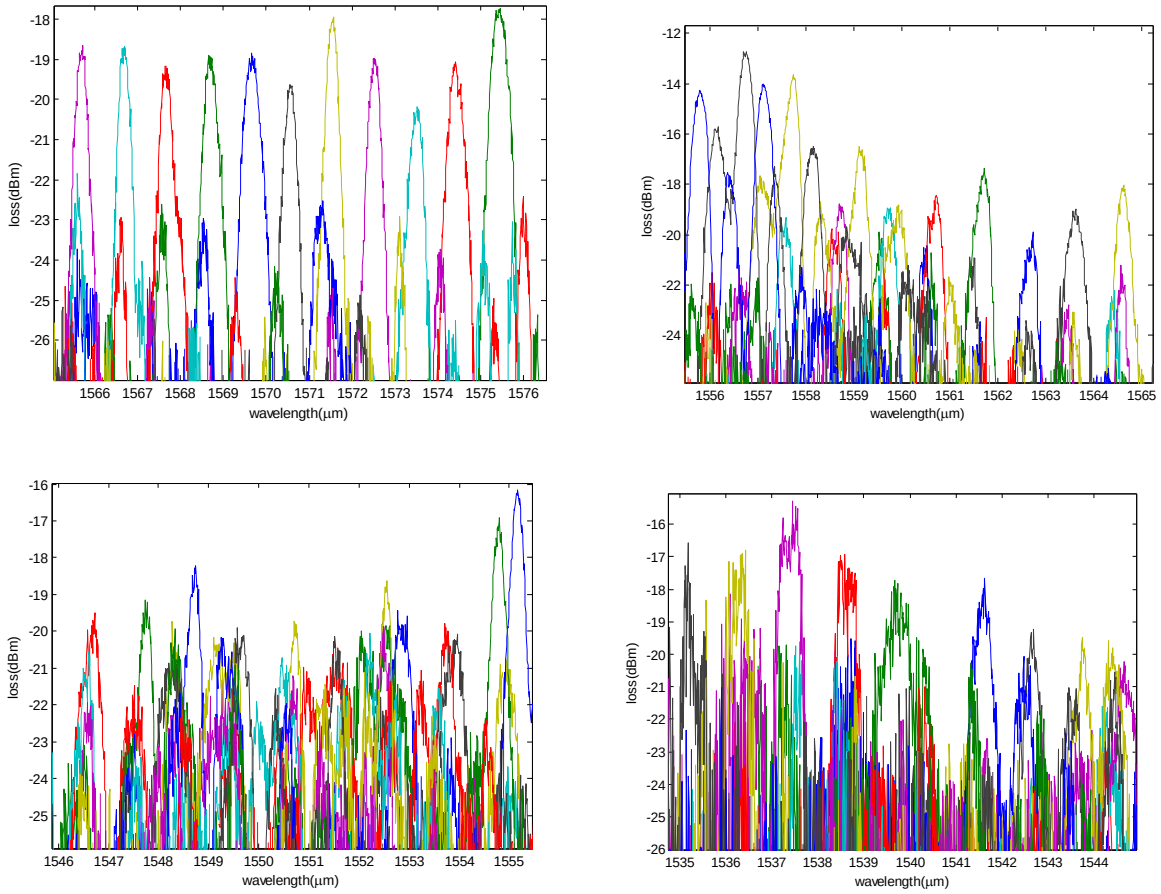

Figure 4.6: Transmission spectra of (a) the 10 first (b) the 10 second (c) the 10 middle (d)the 10 third (e)the 10 fourth output channels of the PCG. Normalization considered

There is great deviation of the measured result from the simulation. One possible reason for the deviation from the simulation results is the roughness of the etched walls. The PCG is very big and has a wide area slab region. Due to fabrication error, or contamination during measurement, there can be some variation on the effective refractive index of the slab region. The diffracted light from the grating, on its way back to the output waveguides can pick some phase in the FPR. This will distort the condition of constructive interference, which obviously can affect the spectral response.

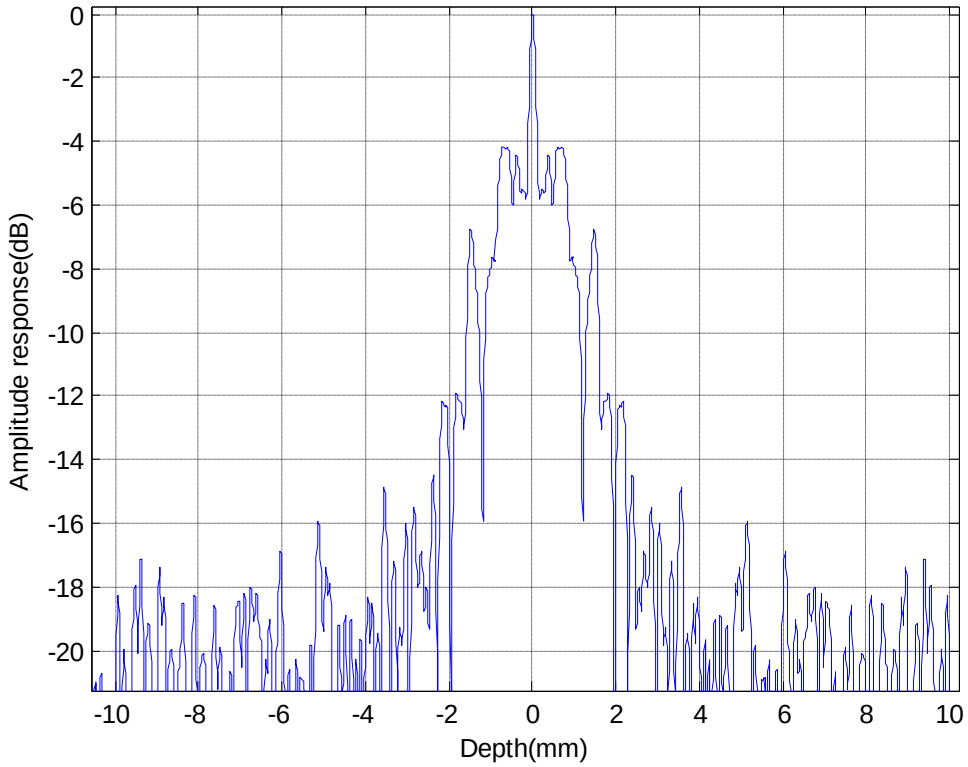

Figure 4.6: Low pass filter characteristics of the PCG spectrometer

Figure shows the low pass filter nature of the spectrometer. The high crosstalk of the PCG spectrometer doesn't affect much the OCT image. As seen from the transfer function of the PCG, it can allow imaging as deep as 500um with a loss of 5dB.

4.3.3 Characterization of the OCT system

We included one 3-D translational stage to the setup used above for mounting the sample to be imaged. We used a tissue paper as the sample to be imaged. Since the noise level of the PCG is very high, we opted to measure the interferogram directly from the reference waveguide using an Optical Spectrum Analyzer. We first measured the OCT output without mounting the sample, and the blue spectrum shown in the figure is obtained. The corresponding Fourier transform is also shown. We used paper as our imaging sample, we mounted it about 100um above the Mach-Zehnder. We got the green spectrum shown in the figure 4.7. As seen, there is no significant difference between the two spectrum. We did two measurements: one without the

sample (the blue curve), the other with the sample (the green curve). There is no significant difference between the spectrum measured by mounting the sample, and without the sample. , the A-scan of the paper does not generate signals that can be distinguished from the background measurement without a sample.

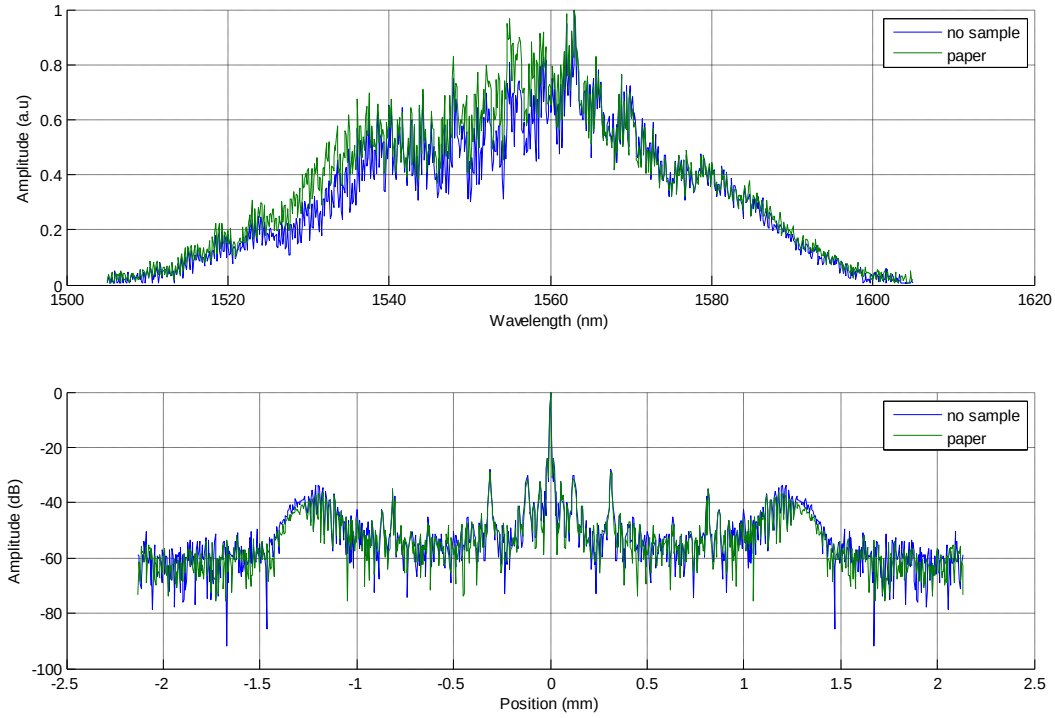

Figure 4.7: OCT measurement results. The upper plot if the amplitude spectrum, the lower one is the Fourier transform of the measured interferogram.

We made analysis of the OCT measurement setup sensitivity by doing some experiments on fiber based OCT. The result is shown in figure 4.8. As can be seen in the figure, the sensitivity is around 60 dB. When it comes to our chip based OCT, there is 31dB loss from the input/output grating couplers and the lower arm of the MZ-interferometer. In the upper arm, we used a simple grating for coupling the light out of the chip and illuminate the sample to be imaged. The loss of this grating is 9dB. For collecting the reflected light from the sample and couple it back to the waveguide, we used same kind of uniform grating. Since the grating is

optimized for coupling from fiber to waveguide, its efficiency is definitely less than for coupling scattered light to a waveguide. The loss is more than 9dB. Thus, our OCT setup incurs a loss of at least 50dB to the OCT signal. This is very close to the 60dB sensitivity of the fiber based OCT. That prevents us from measuring OCT signals from our chip system.

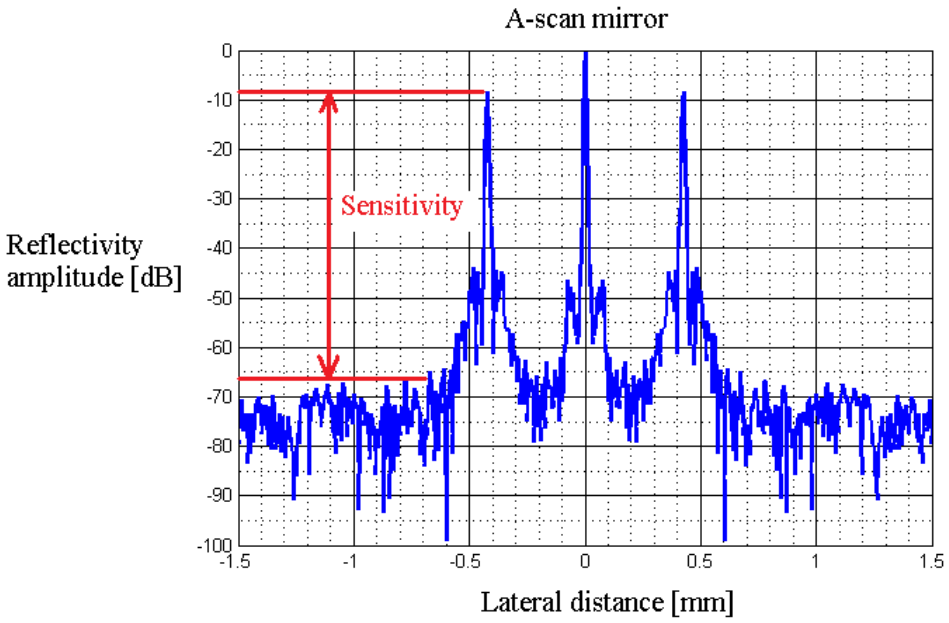

Figure 4.7: Sensitivity of Fiber based OCT

We did two measurements: one without the sample (the blue curve), the other with the sample. As expected from the sensitivity of the system, the A-scan of the paper does not generate signals that can be distinguished from the background measurement without a sample.

Chapter 5

Conclusion

In this thesis, we explored the potential of SOI for implementing a miniaturized OCT system. To this end we proposed a Mach-Zehnder interferometer based FD-OCT on an integrated photonics circuit. The photonic IC consists of waveguides, splitters and combiners forming the MZ, grating couples that effect the communication of the chip with the outside environment, and a Planar Concave Grating (PCG) based spectrometer forming the detection system. All the components are optimized to operate at wavelengths centered at 1550um.

The PCG is designed following the Rowland configuration. It has a channel spacing of 1nm which can allow imaging as deep as $350\mu m$. It has 50 output channels which effectively gives an operation bandwidth of 50nm. This bandwidth can give an axial resolution of $15\mu m$. The fabricated PCG has a foot print of $2.1mm \times 5.1mm$. Measurement is done to characterize the PCG performance. There is discrepancy between the measured results and the simulation. The deviation can be due to some fabrication irregularities and contamination of the chip during measurement. In addition, the simulation assumes some approximations; a much more rigorous analysis can help to design a more optimized PCG demultiplexer.

We studied the potential of a Focusing Grating Coupler (FGC) to constitute the probing element of the OCT system. The FGC is basically a curved and chirped grating. It can couple the light out of the upper arm of the MZ-interferometer and focus it to a point on the sample to be imaged. We simulated an FGC of size $40\mu m \times 40\mu m$ with a focal length of $350\mu m$. The efficiency, the focusing performance, and aberration properties of the FGC are analyzed. The variation of the grating back reflection with wavelength is calculated. The outcoupling efficiency deteriorates at wavelengths where the back reflection peaks. Groove depth of the grating greatly affects the beam profile at the focus plane. The beam spot size increases for deeper grooves.

The FGC can also be used to collect the light reflected from the sample to be imaged and to couple it back to the upper arm of the MZ-interferometer. Further modeling is required to optimize the grating profile so that it can efficiently collect light reflected from a scattering media. This requires analysis of scattering from the inhomogeneous media and correcting for the grating profile accordingly. Due to time constraint FGC simulations were performed after the

chip designs were send for fabrication. These simulations will be useful for the future OCT on a chip designs.

The fabricated photonic ICs for OCT were characterized. These measurements helped us to better understand the SNR requirements and tolerable loss in the system. Multiple reflections within the system have been observed, which may degrade OCT signal. These reflections from the gratings, splitter and combiners have to be optimized in the future designs. Due to high losses in the system and limited SNR of the measurement system, OCT measurements were not technically possible. However, with improved system design and measurement setups, OCT on a chip is feasible and this study experimentally showed the challenges to be care

Appendix I

In this appendix, we calculate the expression for the field values on the surface of the FGC when the wavelength of the input guided wave is different from the design wavelength.

Equation A1 of Joel's paper [33] takes the form

$$I_1(q_y, q_z) = \iint_{-\infty}^{\infty} \zeta(y,z)\exp(-iq_y y)\exp[-i(q_y - \beta)z]dydz$$

where $\zeta(y,z) = \exp[-i(\beta_0 z + k_o R)]$

Here, $\beta_0 = \frac{2\pi}{\lambda_0} n_{eff}$, $k_0 = \frac{2\pi}{\lambda_0} n_c$, $\beta = \frac{2\pi}{\lambda} n_{eff}$

where λ_0 is the design wavelength , and n_c is the index of cover, air.

Thus, I_1 becomes

$$I_1(q_y, q_z) = \iint_{-\infty}^{\infty} \exp\{ik_o F(y,z)\}dydz$$

where $F(y,z) = -R(y,z) - \frac{q_y}{k_o} - \frac{q_z}{k_o} z + (\beta - \beta_o)\frac{z}{z_o}$

To calculate the integral(Born) $I_1(q_y, q_z)$, the method of stationary phase can be applied.

The critical point satisfies the equation:

$$y_o = -\frac{q_y}{k_o} R(y_o, z_o)$$

$$z_o = -\frac{q_y}{k_o} R(y_o, z_o) + \frac{R(y_o, z_o)}{k_o}(\beta - \beta_o)$$

Thus,

$$a = \left.\frac{\partial^2 F(y,z)}{\partial y^2}\right|_{y_o, z_o} = \frac{1}{R}\left[\frac{q_y^2}{k_o^2} - 1\right]$$

$$b = \frac{\partial^2 F(y,z)}{\partial z^2}\bigg|_{y_o,z_o} = \frac{1}{R}\left\{\frac{1}{k_o}[-q_z + (\beta - \beta_o)]^2 - 1\right\}$$

$$c = \frac{\partial}{\partial y}\frac{\partial}{\partial z}F(y,z)|\bigg|_{y_o,z_o} = -\frac{q_y}{Rk_o}\{-q_z + (\beta - \beta_o)\}$$

And, $F(y_o, z_o) = -R_o + \frac{R_o}{k_o^2}(q_y^2 + q_z^2) - \frac{R_o}{k_o^2}(\beta - \beta_o)q_z$

Thus, I_1 becomes

$$I_1(q_y, q_z) = \frac{-2\pi i R_o}{\sqrt{\left[k_o^2 - (q_y^2 + q_z^2) - (\beta - \beta_o)^2 + 2q_z(\beta - \beta_o)\right]}} exp[ik_o F(y_o, z_o)]$$

Therefore,

$$\bar{Q}(q_y, q_z) = \bar{U}(q_y, q_z) I_1(q_y, q_z)$$

with $\bar{U}(q_y, q_z)$ the expressions given in equation eq.48-51 of [Joel].

Thus, eq.A9 of Joel's paper [33] can now be written as :

$$\bar{A}_I(x,y,z) = \eta\left(\frac{1}{2\pi}\right)^2 \iint_{-\infty}^{\infty} \bar{U}(q_y, q_z) I_1(q_y, q_z) \exp(iq_c x) \exp(i\bar{q} \cdot R) dq_y q_z$$

The field at the exit pupil of the FGC then becomes

$$\bar{A}_I(0,y,z) = \eta\left(\frac{1}{2\pi}\right)^2 \iint_{-\infty}^{\infty} g(q_y, q_z) \exp[ik_o f(q_y, q_z)] dq_y q_z$$

where

$$g(q_y, q_z) = \bar{U}(q_y, q_z) \frac{-2\pi i R_o}{\sqrt{\left[k_o^2 - (q_y^2 + q_z^2) - (\beta - \beta_o)^2 + 2q_z(\beta - \beta_o)\right]}}$$

and $f(q_y, q_z) = F(y_o, z_o) + \frac{q_y}{k_o} y + \frac{q_z}{k_o} z$

Again method of stationary phase can be applied to evaluate this integral.

The critical point now becomes:

$$q_{y_o} = -\frac{k_o}{2R_o}y \qquad\qquad q_{z_o} = -\frac{k_o}{2R}z + \frac{1}{2}(\beta - \beta_o)$$

Thus,

$$a = \left.\frac{\partial^2 f(q_y, q_z)}{\partial q_y^2}\right|_{q_{y_o} q_{z_o}} = \frac{2R}{k_o^2}$$

$$b = \left.\frac{\partial^2 f(q_y, q_z)}{\partial q_z^2}\right|_{q_{y_o} q_{z_o}} = \frac{2R}{k_o^2}$$

$$c = \left.\frac{\partial}{\partial q_y}\frac{\partial}{\partial q_z} f(q_y, q_z)\right|_{q_{y_o} q_{z_o}} = 0$$

$$f\left(q_{y_o} q_{z_o}\right) = -R + (\beta - \beta_o)\frac{z}{2k_o} - (\beta - \beta_o)^2 \frac{R}{4k_o^2}$$

$$g\left(q_{y_o} q_{z_o}\right) = \bar{U}\left(q_y, q_z\right) \frac{-2\pi i R}{\sqrt{\left[\frac{k_o^2}{4} - (\beta - \beta_o)\frac{k_o z}{2R} - \frac{(\beta - \beta_o)^2}{4}\right]}}$$

Thus, $\bar{A}_I(0, y, z)$ becomes

$$\bar{A}_I(0, y, z) = \frac{\eta \bar{U}(q_y, q_z)}{\sqrt{\left[\frac{k_o^2}{4} - (\beta - \beta_o)\frac{k_o z}{2R} - \frac{(\beta - \beta_o)^2}{4}\right]}} \exp(-ik_o R) exp\left[i\left\{\frac{(\beta - \beta_o)}{2}z - \frac{(\beta - \beta_o)^2}{4k_o}R\right\}\right]$$

This expression reduces to the form of eq.A13 [Joel] for the case when the wavelength of input guided wave matches the design wavelength, i.e. $\beta = \beta_o$

Appendix II

A python script to calculaate the efficiency of the FGC

```
# reflection vs wavelength for differnt etching depth


------------------------------------------------------
------------------------------------------------------
from camfr import *
from numpy import *
from math import *


#set_lambda(1.55)


n_eff2 = 2.833
L = 40.0
f = 350.0
theta=0.0
pi=3.14146
d = 7
dclad = 1.0
guide_thickness = 0.22
ff = 0.5

set_N(130)
set_polarisation(TE)
set_chunk_tracing(0)
set_degenerate(0)
set_orthogonal(False)

pml = -0.4

set_upper_PML(pml)
set_lower_PML(pml)
SiO2 = Material(1.44)
Si = Material (3.476)
air = Material (1.0)


width = [ , , ,...];  # the distance between consecutive grating lines has to be
imported by calculations
            #from the main grating line equation, and taking into account the
maximum size of the FGC.


m_max = size(width)

#create output file
outfile = open("FGC_test.txt",'wt')


for i in range(0,9):
    groove_depth = 0.01*(i+1);
    unetched_slab = Slab(Si(d-dclad) + SiO2(dclad) + Si(guide_thickness) + air(d))
    etched_slab = Slab(Si(d-dclad) + SiO2(dclad) + Si(guide_thickness -
groove_depth) + air(d + groove_depth))
    for r in range(0,100):
        lamda = 1.5396 + 0.001*r
        set_lambda(lamda)


        slabs =[]
        unetched_slab1 = unetched_slab(ff*width[1])
        etched_slab1 = etched_slab((1-ff)*width[1])
        slabs.append(unetched_slab1)
        slabs.append(etched_slab1)
```

```
        for m in range(1,m_max-1):
            etched_slab1 = etched_slab(0.5*ff*(width[m] + width[m-1]))
            unetched_slab1 = unetched_slab((1-ff)*width[m])
            slabs.append(unetched_slab1)
            slabs.append(etched_slab1)


        slabs.append(unetched_slab1)

        N_slabs = 2*m_max - 1  # total number of slabs


        stack1 = Stack(slabs[0] + slabs[1] + ... + slabs[n]) # appending the slabs
to the stack container, n-is total no. of

        unetched_slab.calc()
        guided = 0
        niguided = 1
        for t in range(0,60):
            if abs(unetched_slab.mode(t).n_eff().imag) < niguided:
                guided = t
                niguided = abs(unetched_slab.mode(t).n_eff().imag)
               # set input for calculating the fields
        inc = zeros(N())
        inc[guided] = 1
        stack1.set_inc_field(inc)


        # calculates the reflection and transmission of the stack, grating
        x0 = d
        x1 = d + 0.220
        eps = 0.001
        input_power_flux = stack1.inc_S_flux(x0,x1,eps)
        output_power_flux = stack1.ext_S_flux(x0,x1, eps)
        R = abs(stack1.R12(guided,guided))
        T = abs(stack1.T12(guided,guided))

        length_grating = stack1.length()

        # calculates efficiency

        x = d + 1.5
        powerup = 0.0 + 0.0*1j
        for z in arange(0.01, length_grating , 0.01):
            powerup +=
0.01*stack1.field(Coord(x,0,z)).E2()*conjugate(stack1.field(Coord(x,0,z)).Hz())




        print >> outfile, lamda, groove_depth, R*R, T*T, powerup.real # powerup.real
gives the efficiency
        outfile.flush()
        print lamda
        free_tmps()
outfile.close()
```

Appendix III

```
     A Matlab code to calculate the field profile on the focal plane of the FGC
% Calculates the field profile of the outcoupled light on the focus profile.
-------------------------------------------------------------------------


function calc_far_field()

clear all;
close all;

W=40.0; L=40.0;   %dimension of the FGC
dz=1;
dy=1;

f=350;     %focal length
theta=0;   % focal point deviation from the vertical axis, x-axis
wg_thickness = 0.22;  % thickness of the Si film
etch_depth = 0.03;

nz=round(0.5*L/dz);
ny=round(0.5*W/dy);
n_eff = 2.833;
lamda=1.55;
n_c=1;           %index of cover, i.e. air
n_f = 3.46;      %index of film, i.e. Si
n_s = 1.466;     % index of substrate, i.e. SiO2
delta_n = n_c^2-n_f^2;5;
eta = 0.5*etch_depth;    % amplitude of grating profile

epsilon_o= 8.85*10^(-12); c=3*10^8;

h=0.5*(2*wg_thickness - etch_depth);     % average height of the waveguide (i.e. the
Si film)
Xo=f*cos(theta*pi/180);
Yo=0.0;                  % alternatively Yo=0.0, can be used to find field profile
along Z axis

Z_max = 80.0;    % maximum length of observation point, over which field profile is
to be calculated
dZ=0.1;
nZ=round(0.5*Z_max/dZ);
nY=nZ;

Ko= 2*pi/lamda*n_c;

Intensity = zeros(2*nZ+1,1);
E_x=zeros(2*nZ+1,1); E_y=zeros(2*nZ+1,1); E_z=zeros(2*nZ+1,1);
global A_Ix A_Iy A_Iz delta_x delta_y delta_z dz dy A_x A_y A_z W L dz dy f theta
wg_thickness etch_depth nz ny n_eff lamda n_c n_f n_s

calc_phase()

Yo=0;
Zo = linspace(-Z_max/2,Z_max/2,2*nZ+1);
%Yo = linspace(-W/2,W/2,2*ny+1);


for j=-nZ:nZ        % iterating over Zo, i.e to calculate field at each point on
focal plane
    p=j+nZ+1;
    Z = j*dZ;
    A_farX=0; A_farY=0; A_farZ=0;
    for s=1:2*nz+1          % to integrate over the z axis
        z=(s-nz-1)*dz;
        for t=1:2*ny+1     % the y component of the double integral
            y=(t-ny-1)*dy;
            r_01 = sqrt(Xo^2 + (Z-z)^2 + (Yo-y)^2);      % vector from any
differential volume element of the FGC to focal point
```

```
            Kernel = -i*f/lamda * exp(i*Ko*r_01)/(r_01^2)*dz*dy;    % Kernel of the
double integral
            A_farX = A_farX + A_x(s,t)*Kernel;
            A_farY = A_farY + A_y(s,t)*Kernel;
            A_farZ = A_farZ + A_z(s,t)*Kernel;
        end
    end
    E_x(p) = E_x(p) + abs(A_farX);
    E_y(p) = E_y(p) + abs(A_farY);
    E_z(p) = E_z(p) + abs(A_farZ);
    Intensity(p)=Intensity(p) + epsilon_o*c*(E_x(p)^2 + E_y(p)^2 + E_z(p)^2);
end

%normalization

max_Ey = max(E_y);
for p=1:2*nZ+1
    E_y(p) = E_y(p) - E_y(p)*(1-1/max_Ey);
end

max_I = max(Intensity);

for p=1:2*nZ+1
    Intensity(p) = Intensity(p) - Intensity(p)*(1-1/max_I);
end


max_I = max(Intensity)
Half_max = 0.5*max_I;

n_left = 1;
while(Intensity(n_left)< Half_max)
    n_left = n_left + 1;
end

n_right=2*nZ+1;

while(Intensity(n_right)< Half_max)
    n_right = n_right - 1;
end

%intensity plot

figure;
plot(Zo,E_x)

figure;
plot(Zo,E_y)

figure;
plot(Zo,E_z)

figure;
plot(Zo,Intensity)


------------------------------------------------------------
------------------------------------------------------------

% calculates the phase at each point of the grating syrface.


function calc_phase()

global A_Ix A_Iy A_Iz delta_x delta_y delta_z dz dy A_x A_y A_z W L dz dy f theta
wg_thickness etch_depth nz ny n_eff lamda n_c n_f n_s Ko
```

```
h=0.5*(2*wg_thickness - etch_depth);   % average height of the waveguide (i.e. the
Si film)

delta_n = n_c^2-n_f^2;
eta = 0.5*etch_depth;    % amplitude of grating profile

Ko= 2*pi/lamda*n_c;      % wave vector in cover (air)
A=1;
global A_Ix  A_Iy  A_Iz  delta_x delta_y delta_z dz dy A_x A_y A_z

A_x = zeros(2*nz+1,2*ny+1); A_y=zeros(2*nz+1,2*ny+1); A_z = zeros(2*nz+1,2*ny+1);
for k=-nz:nz      % looping over the length of the FGC, along z
    s=k+nz+1;     % to get a positive number for the matrix index
    for j=-ny:ny
        t=j+ny+1;
        calc_A(j,k); % calculates the A at any point,(y=j*dy,z=k*dz)on the FGC
surface
        A_x(s,t)=A_Ix; A_y(s,t)=A_Iy; A_z(s,t) = A_Iz;  % stores the values so that
can be used in calc_far_field() function
    end
 end

------------------------------------------------------------
------------------------------------------------------------

% calculates the field value at any point on the grating surface


function calc_A(j,k)  % j- y coordinate, k- z coordinate

global A_Ix A_Iy A_Iz delta_x delta_y delta_z dz dy A_x A_y A_z W L dz dy f theta
wg_thickness etch_depth nz ny n_eff lamda n_c n_f n_s

h=0.5*(2*wg_thickness - etch_depth); % average height of the waveguide (i.e. the Si
film)

alpha = 0.5*0.079387214; % the intensity decay constant, obtained from CAMFR
simulation

delta_n = n_c^2-n_f^2;
eta = 0.5*etch_depth; % amplitude of grating profile

Ko= 2*pi/lamda*n_c;  % wave vector in cover (air)
A=1;

y=j*dy ;
z= k*dz; %j =y, k=z
R=sqrt((f*cos(theta*pi/180))^2+y^2+(f*sin(theta*pi/180)-z)^2); % magnitude of vector
from the point of calculation to focal point


delta_n = n_c^2-n_f^2;
q_y= -Ko*y/R;  q_z=Ko*(f*sin(theta*pi/180)-z)/R; % q is the projection of the
wavevector from any point (on the FGC surface) on the FGC surface.(y-z plane)
q=sqrt(q_z^2+q_y^2);

q_c=sqrt(n_c*Ko^2-q^2); q_f=sqrt(n_f*Ko^2-q^2); q_s=sqrt(n_s*Ko^2-q^2); % transverse
propagation constants i.e. in x direction perpendicular to layers
rho=zeros(3,3);
rho_coeff= (n_s - n_f)/((q_s+q_f)*(n_s/q_s + n_f/q_f)); %coefficient of the rho
matrix
F=(q_f-q_s)/(q_f+q_s)*exp(i*q_f*h)+exp(-i*q_f*h);

% calculates the rho matrix elements
rho(1,1)=0; rho(1,2)=q_y/q_f*(1-q^2/(q_s*q_f)); rho(1,3)=q_z/q_f*(1-q^2/(q_s*q_f));
rho(2,1)=0; rho(2,2)=(q_y^2-q_z^2)/(q_s*q_f)-1;rho(2,3)=2*q_y*q_z/(q_s*q_f);
```

```
     A Matlab code to calculate the field profile on the focal plane of the FGC
rho(3,1)=0; rho(3,2)=2*q_y*q_z/(q_s*q_f); rho(3,3)=-(q_y^2-q_z^2)/(q_s*q_f)-1;

D=(rho(2,2)*exp(i*q_f*h)+exp(-i*q_f*h))*(rho(3,3)*exp(i*q_f*h)+exp(-i*q_f*h))-rho(2,
3)*rho(3,2)*exp(i*2*q_f*h);

%calculates the sigma matrix elements
sigma=zeros(3,3);
sigma(1,1)=0; sigma(1,2)=F*(q_y/q_f)*exp(i*q_c*h)/D;
sigma(1,3)=F*q_z/q_f*exp(i*q_c*h)/D;
sigma(2,1)=0; sigma(2,2)=(rho(3,3)*exp(i*q_f*h)+exp(-i*q_f*h))*exp(i*q_c*h)/D;
sigma(2,3)=-rho(2,3)*exp(i*q_f*h)*exp(i*q_c*h)/D;
sigma(3,1)=0; sigma(3,2)=-rho(3,2)*exp(i*q_f*h)*exp(i*q_c*h)/D;
sigma(3,3)=(rho(2,2)*exp(i*q_f*h)+exp(-i*q_f*h))*exp(i*q_c*h)/D;


%calculates the tau matrix
tau=zeros(3,3);
tau=rho*sigma;

%calculates the alpha\s
alpha_1y =
-(q_y^2/q_c+q_c)*exp(i*q_c*h)-(q_y*tau(1,2)-q_f*tau(2,2))*exp(i*q_f*h)-(q_y*sigma(1,
2)+q_f*sigma(2,2))*exp(-i*q_f*h);
alpha_1z =
-q_y*q_z/q_c*exp(i*q_c*h)-(q_y*tau(1,3)-q_f*tau(2,3))*exp(i*q_f*h)-(q_y*sigma(1,3)+q
_f*sigma(2,3))*exp(-i*q_f*h);
alpha_2y =
-q_y*q_z/q_c*exp(i*q_c*h)-(q_z*tau(1,2)-q_f*tau(2,3))*exp(i*q_f*h)-(q_z*sigma(1,2)+q
_f*sigma(3,2))*exp(-i*q_f*h);
alpha_2z = -(q_z^2/q_c
+q_c)*exp(i*q_c*h)-(q_z*tau(1,3)-q_f*tau(3,3))*exp(i*q_f*h)-(q_z*sigma(1,3)+q_f*sigm
a(3,3))*exp(-i*q_f*h);

U_y=alpha_2z/(alpha_1y*alpha_2z-alpha_2y*alpha_1z)*i*delta_n*Ko^2*A;
U_z=-alpha_2y/(alpha_1y*alpha_2z-alpha_2y*alpha_1z)*i*delta_n*Ko^2*A;
U_x=-1/q_c*(q_y*U_y+q_z*U_z);

decay = exp(-alpha*(0.5*L+z)); %decay =
exp(-0.5*alpha*(0.5*L+z+2*f*sin(theta*pi/180)));

A_Ix=decay*eta*U_x*exp(-i*Ko*R); A_Iy=decay*eta*U_y*exp(-i*Ko*R);
A_Iz=decay*eta*U_z*exp(-i*Ko*R);

-----------------------------------------------------------------
-----------------------------------------------------------------
```

Appendix IV

```
              A python script to generate the mask layout of the PCG
-----------------------------------------------------------------
# semere_route_pcg.py # it is a class that routes the PCG

from picazzo.routing.to_line import *
from picazzo.routing.connect import *
from picazzo.basic.port_element_structures import *
from picazzo.wg.bundle import *


class _route_pcg_outputs(processed_item, autoname_dynamic_port_structure):
    pcg_transformation = transformation_property("__pcg_transform")
    def __init__(self, pcg, port_indices_to_right, y_base = None, pcg_transformation
= None, library=None):
        self.pcg = pcg
        self.port_indices_to_right = port_indices_to_right
        self.y_base = y_base
        self.pcg_transformation = pcg_transformation
        autoname_dynamic_port_structure.__init__(self, library)

    @classmethod
    def __str_name__(self, pcg, port_indices_to_right, y_base = None,
pcg_transformation = None, library=None):
        if y_base == None:
            YB = "None"
        else:
            YB = str(int(y_base *1000))
        if pcg_transformation == None:
            TR = 0
        else:
            TR = hash(pcg_transformation.id_string())
        return "%s_%s_PI%s_Y%s_T%d" % (self.__name_prefix__, pcg.name,
"_".join([str(p) for p in port_indices_to_right]), YB, TR)
    def __calc_name__(self):
        return self.__str_name__(self.pcg, self.port_indices_to_right, self.y_base,
self.pcg_transformation)

    def __calc_common__(self):
        self += el_sref(self.pcg, (0.0, 0.0), self.pcg_transformation).flat_copy()
        for R in self.routes:
            self += R

    def __calc_ports__(self):
        P = port_list()
        for R in self.routes:
            P+= R.out_ports
        self.ports = P

class _route_pcg_outputs_bundled(_route_pcg_outputs):

    def __calc_common__(self):
        self += el_sref(self.pcg, (0.0, 0.0), self.pcg_transformation).flat_copy()
        for B in self.bundles:
            R = [self.routes[i] for i in B]
            self += wg_el_bundle_waveguides(R)


class route_pcg_outputs_top(_route_pcg_outputs_bundled):
    __name_prefix__ = "RT"
    def __calc_info__(self):
        self.routes = []
        SI = self.pcg.size_info().transform(self.pcg_transformation)
        PL = self.pcg.ports.y_sorted().transform_copy(self.pcg_transformation)
        x_base_left = None
        x_base_right = None
        y_base = self.y_base
        if y_base == None:
            y_base = SI.top + WG_TRENCH_WIDTH + WG_SPACING
```

```
        other_bundle = []
        for p in PL.y_sorted_backward():
            i = PL.index(p)
            if i in self.port_indices_to_right:
                if abs((p.angle_deg+90)%360-90) <=90: #pointing right
                    R = route_to_right(p)
                elif x_base_left == None:
                    R = route_to_top(p)
                    R.end_straight = 0.01
                    R2 = route_to_right_at_y(R.out_ports[0], y_base)
                    R2.end_straight += max(0.0, SI.right - R2.out_ports[0].x ) #
modify
                    #if i < max(self.port_indices_to_right)/2:
                    R2.end_straight +=i*3.0
                    #else:
                     #   R2.end_straight += (max(self.port_indices_to_right)-i)*3.0
                    R += R2
                    y_base += WG_SPACING
                    x_base_left = R.size_info().left - WG_SPACING-WG_WIRE_WIDTH
                else:
                    R = route_to_top_at_max_x(p, x_base_left)
                    R.end_straight = 0.01
                    x_base_left = R.out_ports[0].x - WG_SPACING - WG_WIRE_WIDTH
                    R2 = route_to_right_at_y(R.out_ports[0], y_base)
                    R2.end_straight += max(0.0, SI.right - R2.out_ports[0].x )
                    #if i < max(self.port_indices_to_right)/2:
                    R2.end_straight +=i*3.0
                    #else:
                     #   R2.end_straight += (max(self.port_indices_to_right)-i)*3.0
                    R += R2
                    y_base += WG_SPACING
            else:
                if abs((p.angle_deg+90)%360-90) >90: #pointing left
                    R = route_to_left(p)
                    R.end_straight = 500.0
                elif x_base_right == None:
                    R = route_to_top(p)
                    R.end_straight = 0.01
                    R2 = route_to_left_at_y(R.out_ports[0], y_base)
                    R2.end_straight += max(0.0, R2.out_ports[0].x - SI.left)
                    #if i < max(self.port_indices_to_right)/2:
                    R2.end_straight +=i*3.0
                    #else:
                     #   R2.end_straight += (max(self.port_indices_to_right)-i)*3.0
                    R += R2
                    y_base += WG_SPACING
                    x_base_right = R.size_info().right + WG_SPACING+WG_WIRE_WIDTH
                else:
                    R = route_to_top_at_min_x(p, x_base_right)
                    R.end_straight = 0.01
                    x_base_right = R.out_ports[0].x + WG_SPACING+WG_WIRE_WIDTH
                    R2 = route_to_left_at_y(R.out_ports[0], y_base)
                    R2.end_straight += max(0.0, R2.out_ports[0].x - SI.left)
                    #if i < max(self.port_indices_to_right)/2:
                    R2.end_straight +=i*3.0
                    #else:
                     #   R2.end_straight += (max(port_indices_to_right)-i)*3.0
                    R += R2
                    y_base += WG_SPACING
                other_bundle += [i]

            self.routes += [route_connector_rounded_expanded(R)]
            self.bundles = [self.port_indices_to_right, other_bundle]

----------------------------------------------------------------
----------------------------------------------------------------
```

```
# this class generates the PCG geometry, dimension of the grating facets has to be
fed from matlab

from picazzo.slab.aperture_layout import *
from picazzo.wg.aperture_multi import *
from semere.semere_route_pcg import *
from Joost.detector_pcg import *
from picazzo.fibcoup.uniform import *
from picazzo.filters.pcg import *
from tools.cmdline import *
from picazzo.wg.basic import *
from picazzo.fxt.column import *

import sys

# This file contains the actual parameters for a design, and constructs the
individual PCG objects

def my_pcg_design():

    #pole of rowland circle (position and angle)
    pole_vector = gds_vector((2980.567540221047,0.0), 221.0) # Angle: 180+a ;
(x=straal*cos(a),y=0.0)

    # apertures
    aperture_angles =[ , , ] # input from matlab code


aperture_vectors = aperture_layout_rowland(pole_vector, radius = 1974.645359173297,
angles = aperture_angles)
aperture = shallow_wg_aperture_merged( vectors = aperture_vectors,
                                       aperture_width = 2.25,
                                       taper_length = 30.0,
                                         )

facets = pcg_facets_from_shape[] # calculated from matlab code, it is a an array of
the PCG grating facets

grating = pcg_from_facet_flat(pole_vector, facets)

    pcg = pcg_demux([aperture], grating)

    pcg_r = route_pcg_outputs_top(pcg, port_indices_to_right = range (0,50),
pcg_transformation = gds_v_mirror())
    pcg_r.left_ports.y_sorted()
    return pcg_r

parse_cmdline("WG")

set_grid(5E-9)
set_unit(1E-6)

layout = fxt2_column("AWG")
layout.straighten()

layout += my_pcg_design()

layout.straighten()
layout.add_emptyline(3)

my_lib = gds_library("Sem", 1E-6, 5E-9)
my_lib.add(layout)
my_lib.calc()
out = gds_output_gdsii(stdout)
out.write(my_lib)
--------------------------------------------------------------------------------
```

List of Figures

References

[1] D. Huang, et.l "Optical coherence tomography", Science 254, 1178-1181 (1991).

[2] http://www.md-ltd.co.uk/oct/index.htm / accessed April 27, 2008

[3] A F Fercher, et al.(2003), "Optical Coherence Tomography principles and applications", Rep. Prog. Phys. Issue 66, pp 239–30.3

[4] Bass, Eric W. Van Stryland, David R. Williams, William L. Wolfe, "Handbook of Fundamentals, Techniques, & Design" , 2nd ed, McGRAW-HILL , INC , Vol I

[5] P H Tomlins,et al.(2005),"Theory, developments and applications of optical coherence tomography", J. Phys. D: Appl. Phys. Issue 38, pp 2519–2535.

[6] Joseph W.Goodman, (1985),"Statistical Optics", 3rd edition, chapter 3.

[7] Lihong V. Wang, (2007), "Biomedical Optics: principles and imaging",Wiley, chapter 9

[8] Maciej Wojtkowski, et al.(2002), "In vivo human retinal imaging by Fourier domain optical coherence tomography", Journal of Biomedical Optics 7(3), 457–463.

[9] Tony KO, et al.(2004), "Ultrahigh resolution optical coherence tomography imaging with a broadband superluminescent diode source", Opt. Express, Vol. 12, Issue 10, pp. 2112-2119.

[10] Wolfgang Drexler,(2004) "Ultra-high resolution optical coherence tomography", J.Biomedical Optics, Vol. 9, No. 1 47.

[11] Eugeren Hecht, "Optics", 4th edition.

[12] Choma MA, et al. (2003), "Sensitivity advantage of swept-source and Fourier-CBVdomain optical coherence tosmography." Opt. Express Vol . 11 no.18 pp 2183-2189.

[13] C. Dorrer, et al.(2000), "Spectral resolution and sampling issues in Fourier-transform spectral interferometry," J. Opt. Soc. Am. B 17, 1795-1802.

[14] W. Bogaerts, et al. (2006), Basic structures for photonic integrated circuits in Silicon-on-insulator,Optics Express (invited), 12(8), p.1583-1591.

[15] P. Dumon, et al.(2006), Compact wavelength router based on a Silicon-on-insulator arrayed waveguide grating pigtailed to a fiber array,Optics Express, 14(2), p.664-669.

[16] Roelkens G, et al.(2005), "Efficient silicon-on-insulator fiber coupler fabricated using 248-nm-deep UV lithography." IEEE Photonics Technology Letters 17 (12): 2613-2615.

[17] Baets, R, et al. (2005), "Silicon-on-insulator based nano-photonics: Why, How, What for?" Proc. of IEEE International Conference on Group IV Photonics. 21-23 Sept. p168 – 170.

[18] B. Luyssaert, et al. (2005), "A Compact Horizontal Spot-Size Converter Realized in Silicon-on-Insulator",IEEE Photonics Technology Letters, 17(1), p.73-75.

[19] J. Brouckaert, et al. (2007), "Planar Concave Grating Demultiplexer Fabricated on a Nanophotonic Silicon-on-Insulator Platform" ,Journal of Lightwave Technology, 25(5), p.1269-1275

[20] Erwin G. Loewen, (1997), "Diffraction Gratings and Applications (Optical Engineering)", 1st edition, chapter 7.

[21] H. A. Rowland,et al.(1882),"Preliminary notice of the results accomplished in the manufacture and theory of gratings for optical purpose," Philos. Mag., vol. 13, pp. 469–474.

[22] M. Born and E. Wolf, Principles ofOptics . New York: Pergamon, 1980, ch. 8.

[23] K. A. McGreer, (1996), "Theory of concave gratings based on a recursive definition of facet positions", APPLIED OPTICS, Vol. 35, No. 30.

[24] D. Chowdhury,(2000) "Design of low-loss and polarization-insensitive reflection grating-based planar demultiplexers," IEEE J. Sel. Topics Quantum Electron., vol. 6, no. 2, pp. 233–239,

[25] F. J. M. J. Maessen et al. (2004), "Dispersion of monochromators",J. Anal. Chem.

[26] K. A. McGreer ,(1995), "Diffraction from Concave Gratings in Planar Waveguides", IEEE PHOTONICS TECHNOLOGY LE'ITERS, VOL. 7, NO. 3.

[27] Dirk Taillaert, (2004), "Grating Couplers as Interface between Optical Fibres and Nanophotonic Waveguides",Ghent University, Phd, thesis http://photonics.intec.ugent.be/publications/phd.asp?ID=136

[28] Toshiaki Suhara, et al.(1982)," Integrated Optics Components and Devices Using Periodic Structures", J.Quantum Elect., vol 22, 6,845-876.

[29] Shogo Ura, et al. (1986), "An Integrated-Optic Disk Pickup Device",J. LightwaveTech, vol.4, no.7,913-918.

[30] S. J. Sheard, et al.(1993) "**Integrated-optic implementation of a confocal scanning optical microscope**"J. LightwaveTech. 11, 1400.

[31] Shogo Ura, et al.(1989), "Integrated-optic interferometer position sensor" J. Lightwave Tech.7, 270-273.

[32] P.Bienstman,(2008), "CAMFR , Cavity Modeling Framework", http://camfr.sourceforge.net/index.html

[33] Joel Seligson, (1988),"Modeling of a focusing grating coupler using vector scattering theory", Applied Optics , Vol. 27, No. 4.

[34] Peter Bienstman, (2001),"Rigorous and efficient modelling of wavelength scale photonic components" ",Ghent University, Phd, thesis.

http://photonics.intec.ugent.be/publications/PhD.asp?ID=104

[35] Joseph W.Goodman "Introduction to Fourier Optics", McGraw-Hill, 2nd ed., chapter 3

[36] http://photonics.intec.ugent.be/research/facilities/design/ipkiss/default.htm

[37] W.Bogaerts, (2004), "Nanophotonic Waveguides and Photonic Crystals in Silicon-on-Insulator", Phd thesis, Ghent University.

http://photonics.intec.ugent.be/publications/PhD.asp?ID=135

[38] W. Bogaerts, et al. (2004), "Basic structures for photonic integrated circuits in Silicon-on-insulator", Optics Express, 12(8), 1583-1591.

[39] W. Bogaerts, et al. (2006), "Compact wavelength-selective functions in silicon-on-insulator photonic wires," IEEE J. Sel. Topics QuantumElectron., vol. 12, no. 6, pp. 1394–1401.

[40] W. Bogaerts, et al. (2004), "Basic structures for photonic integrated circuits in silicon-on-insulator," Opt. Express, vol. 12, no. 8, pp. 1583–1591.

[41] D. Taillaert, et al. (2006), "Grating couplers for coupling between optical fibers and nanophotonic waveguides," Jpn. J. Appl. Phys., vol. 45, no. 8A, pp. 6071–6077.